Effects of Intraligand Electron Delocalization, Steric Tuning, and Excited-State Vibronic Coupling on the Photophysics of Aryl-Substituted Bipyridyl Complexes of Ru(II)

Niels H. Damrauer, Thomas R. Boussie, Martin Devenney, and James K. McCusker*

Contribution from the Department of Chemistry, University of California at Berkeley, Berkeley, California 94720-1460

Received April 25, 1997[⊗]

Abstract: The synthesis and photophysical characterization of a series of aryl-substituted 2,2′-bipyridyl complexes of Ru^{II} are reported. The static and time-resolved emission properties of $[Ru(dpb)_3](PF_6)_2$, where dpb is 4,4′-diphenyl-2,2′-bipyridine, have been examined and are contrasted with those of $[Ru(dmb)_3](PF_6)_2$ (dmb = 4,4′-dimethyl-2,2′-bipyridine). It is shown through analysis of electrochemical data and detailed fitting of the emission spectrum that the unusually large radiative quantum yield for $[Ru(dpb)_3](PF_6)_2$ in CH_3CN solution at room temperature is due to reduction of the degree of geometric distortion along primarily ring-stretch acceptor mode coordinates relative to other molecules in this class. It is proposed that the ^{3}MLCT excited state of $[Ru(dpb)_3]^{2+}$ is characterized by a ligand conformation in which the 4,4′-phenyl substituents are coplanar with the bipyridyl fragment, leading to extended intraligand electron delocalization and a smaller average change in the C−C bond length upon formation of the excited state as compared to $[Ru(dmb)_3]^{2+}$. These conclusions are further supported by photophysical data on several new molecules, $[Ru(dptb)_3](PF_6)_2$ (dptb = 4,4′-di-*p*-tolyl-2,2′-bipyridine), $[Ru(dotb)_3](PF_6)_2$ (dotb = 4,4′-di-*o*-tolyl-2,2′-bipyridine), and $[Ru(dmesb)_3](PF_6)_2$ (dmesb = 4,4′-dimesityl-2,2′-bipyridine). The systematic increase in steric bulk provided by this ligand series results in clear trends in k_r, k_{nr}, and S_M (the Huang−Rhys factor), consistent with the delocalization model. In addition, time-resolved resonance Raman data reveal frequency shifts in ring-stretch modes across the series supporting the notion that, as the steric bulk of the ligand increases, the ability for the peripheral phenyl rings to become coplanar with the bipyridyl fragment is hindered. Ab initio calculations employing Hartree−Fock and second-order perturbation theory on neutral and anionic 4-phenylpyridine, put forth as a model for the ground and excited states of $[Ru(dpb)_3]^{2+}$, are also reported. These calculations suggest a canted geometry for the ground state, but a considerable thermodynamic driving force for achieving planarity upon reduction of the ligand. The canted ground-state geometry is also observed in the single-crystal X-ray structure of the mixed-ligand complex $[Ru(dmb)_2(dpb)](PF_6)_2$. Finally, consideration of how this system evolves from the Franck−Condon state to the planar thermalized ^{3}MLCT state is discussed with regard to the possibility of time-resolving the onset of extended electron delocalization in the excited state by using ultrafast spectroscopy.

Introduction

Research on the photophysics and photochemistry of transition metal complexes continues to be of interest in the chemical community.[1−3] For transition metal complexes that exhibit charge transfer transitions, the electronic structure of the ligand plays a crucial role in determining the photophysical properties of the molecule. For the general case of a metal−ligand (M−L) chromophore, excitation in the region of a MLCT absorption results in formal oxidation of the metal center and reduction of the ligand (eq 1).

$$[M^{II}(L)_3]^{2+} \xrightarrow{(h\nu)} [M^{III}(L^-)(L)_2]^{2+} \qquad (1)$$

Typically, the electron is transferred from what is nominally a metal-based d orbital to an antibonding orbital of the ligand.[4] Changes in the ligand which influence either the basicity of the donor or the energetics of the unoccupied orbitals will therefore have an impact on the excited-state properties of the molecule. Exploitation of these effects has served as the basis for synthetic tuning of excited-state properties, an area that has become an important focal point of recent research efforts on approaches to solar energy conversion.[5−7] One aspect of transition metal chemistry that makes it attractive in this context is the geometric and electronic structural diversity that can be achieved through synthetic means. This, coupled with the success of the energy gap law for describing the non-radiative excited-state decay rates of molecules,[8,9] has made synthesis a viable tool for manipulating the excited-state properties of metal complexes. This innate tunability has been exemplified best in polypyridyl complexes of Ru^{II}, Os^{II}, and, to a lesser extent, Re^{I}.[10−13]

[⊗] Abstract published in *Advance ACS Abstracts,* August 15, 1997.

(1) Roundhill, D. M. *Photochemistry and Photophysics of Metal Complexes*; Plenum Press: New York, 1994.

(2) Ferraudi, G. J. *Elements of Inorganic Photochemistry*; Wiley and Sons, Inc.: New York, 1988.

(3) Adamson, A.; Fleischauer, P. D. *Concepts in Inorganic Photochemistry*; Wiley-Interscience, Wiley and Sons, Inc.: New York, 1975.

(4) For a detailed calculation of the electronic structure of $[Ru(bpy)_3](PF_6)_2$, a prototype of this class of molecules, see: Daul, C.; Baerends, E. J.; Vernooijs, P. *Inorg. Chem.* **1994**, *33*, 3538.

(5) Meyer, T. J. *Acc. Chem. Res.* **1989**, *22*, 1048.

(6) Mirkin, C. A.; Ratner, M. A. *Annu. Rev. Phys. Chem.* **1992**, *43*, 719.

(7) Gust, D.; Moore, T. A.; Moore, M. A. *Acc. Chem. Res.* **1993**, *26*, 198.

(8) Treadway, J. A.; Loeb, B.; Lopez, R.; Anderson, P. A.; Keene, F. R.; Meyer, T. J. *Inorg. Chem.* **1996**, *35*, 2242.

(9) Kober, E. M.; Casper, J. V.; Lumpkin, R. S.; Meyer, T. J. *J. Phys. Chem.* **1986**, *90*, 3722.

(10) Connolly, J. S.; Bolton, J. R. *Photoinduced Electron Transfer*; Fox, M. A., Chanon, M., Eds.; Elsevier: Amsterdam, 1988; Vol. Part D.

S0002-7863(97)01321-8 CCC: $14.00

Work in this laboratory focuses on the connection between the electronic and geometric structure of transition metal complexes and their physiochemical properties following photon absorption; our particular emphasis is on ultrafast dynamics. We have recently published a report[14] on the temporal evolution of the Franck-Condon state of $[Ru(bpy)_3]^{2+}$ wherein it was proposed that the observation of ^{3}MLCT excited state formation on the order of ca. 100 fs following ^{1}MLCT ← $^1A_1$ excitation implies the importance of short time scale nonequilibrium dynamics for understanding and ultimately predicting the photophysical and photochemical properties of molecular systems. We are now extending this work to examine compounds of differing electronic and geometric structure to assess how changes in such characteristics manifest themselves in molecular dynamics. This paper describes the synthesis, static, and nanosecond time-resolved spectroscopy of a series of aryl-substituted bipyridyl complexes of Ru^{II}. In addition to providing the necessary foundation for ultrafast studies, the compounds described herein reveal new insights into the influence of electron delocalization on the excited-state properties of molecules. We show that it is possible to control the extent of this delocalization through synthetic modifications of the molecule, thereby providing an alternate means—in addition to well-established energy gap manipulations—by which the excited-state properties of molecules can be tuned. Finally, the conclusions drawn from the data are discussed in terms of the excited-state vibronic coupling implicit in the Franck−Condon evolution of these systems, as well as the potential for observing in real time the onset of electronic delocalization in a molecule.

Experimental Section

General. All reagents and materials from commercial sources were used as received. Solvents were purchased from either Aldrich or Fisher. The ligands 4,4′-dimethyl-2,2′-bipyridine (dmb) and 4,4′-diphenyl-2,2′-bipyridine (dpb) were purchased from Aldrich Chemical Co. $Ru(DMSO)_4Cl_2$[15] and 4,4′-dibromo-2,2′-bipyridine[16] were prepared according to previously published procedures. All syntheses were performed under Ar unless otherwise noted. ^{1}H and ^{13}C NMR spectra were recorded on either a Bruker AMX 300 (300 MHz) or a AMX 400 (400 MHz) spectrometer. All chemical shifts are referenced to residual solvent signals as internal standards previously referenced to TMS, with high-frequency shifts recorded as positive. Elemental analyses and mass spectra were obtained through the Analytical Facilities, University of California at Berkeley. MS measurements used standard FAB conditions for ligands and ESMS for metal complexes. All spectra agreed with appropriate simulations.

Suzuki Couplings: 4,4′-Diaryl-2,2′-bipyridine Ligand Syntheses. A solution of 4,4′-dibromo-2,2′-bipyridine (314 mg, 1.00 mmol) and $Pd(PPh_3)_4$ (58 mg, 0.050 mmol) in 5 mL of degassed toluene was placed in a 50-mL Schlenk tube and combined with a solution of the boronic acid (2.50 mmol) and Na_2CO_3 (424 mg, 4.00 mmol) in 5 mL of degassed 4:1 H_2O/CH_3OH. The biphasic mixture was heated to 100 °C with rapid stirring until TLC showed complete reaction (1−24 h). The reaction mixture was added to a separatory funnel and washed with 3 × 50 mL of Et_2O. The combined organic washes were filtered and dried over Na_2SO_4, and the solvent was removed by rotary evaporation. The resultant material was chromatographed on silica gel with 5−20% ethyl acetate/hexanes eluent. After removal of trace biphenyl products, the disubstituted bipyridines eluted cleanly and were isolated as white powders by rotary evaporation of the solvent.

(a) 4,4′-Di-*o*-tolyl-2,2′-bipyridine (dotb). Yield: 292 mg (87%). ^{1}H NMR ($CDCl_3$): δ 2.34 (s, 6 H), 7.25−7.35 (m, 10H), 8.46 (s, 2H), 8.71 (d, 2H, J = 5.0 Hz). ^{13}C NMR ($CDCl_3$): δ 20.7, 122.2, 124.6, 126.4, 128.7, 129.7, 130.9, 135.4, 139.7, 149.3, 151.2, 156.4. Anal. Calcd for $C_{24}H_{20}N_2$: C, 85.68; H, 5.99; N, 8.33. Found: C, 84.88; H, 5.99; N, 8.06. MS (FAB): *m/z* 335 ($M - H^+$, 100%).

(b) 4,4′-Di-*p*-tolyl-2,2′-bipyridine (dptb). Yield: 232 mg (69%). ^{1}H NMR ($CDCl_3$): δ 2.39 (s, 6 H), 7.21 (d, 4H, J = 8.0 Hz), 7.45 (dd, 2H, J = 5.1, 1.7 Hz), 7.60 (d, 4H, J = 8.1 Hz), 8.21 (m, 4H). ^{13}C NMR ($CDCl_3$): δ 21.3, 119.0, 121.4, 127.0, 129.8, 135.3, 139.2, 149.2, 149.2, 156.7. Anal. Calcd for $C_{24}H_{20}N_2$: C, 85.68; H, 5.99; N, 8.33. Found: C, 84.67; H, 5.97; N, 8.16. MS (FAB): *m/z* 336 (M^+, 100%).

(c) 4,4′-Dimesityl-2,2′-bipyridine (dmesb). Yield: 321 mg (82%). ^{1}H NMR ($CDCl_3$): δ 2.05 (s, 12H), 2.34 (s, 6H), 6.96 (s, 4H), 7.13 (d, 2H, J = 4.8 Hz), 8.31 (s, 2H), 8.70 (d, 2H, J = 4.8 Hz). ^{13}C NMR ($CDCl_3$): δ 21.0, 21.4, 122.5, 125.1, 128.6, 135.4, 136.8, 137.7, 149.8, 151.0, 156.7. Anal. Calcd for $C_{28}H_{28}N_2$: C, 85.67; H, 7.19; N, 7.14. Found: C, 84.50; H, 7.14; N, 6.89. MS (FAB): *m/z* 391 ($M - H^+$, 100%).

Ruthenium Complexes. A solution of $Ru(DMSO)_4Cl_2$ (48.4 mg, 0.0100 mmol) and the bipyridine ligand (0.033 mmol) in 10 mL of 95% EtOH were heated at reflux under Ar for 24 h. After the mixture was cooled to room temperature, the solvent was removed and the solid dissolved in a small amount of CH_3CN. Addition of a 10-fold excess of NH_4PF_6 in H_2O resulted in the formation of an insoluble orange solid that was filtered and collected to yield the PF_6 salts as orange powders. Tris complexes with aryl-substituted bipyridines were twice recrystallized with pentane diffusion into THF. $[Ru(dmb)_3](PF_6)_2$ was twice recrystallized by Et_2O diffusion into CH_3CN, and $[Ru(dmb)_2(dpb)](PF_6)_2$ was recrystallized by slow evaporation of CH_3CN from toluene.

(a) Tris(4,4′-dimethyl-2,2′-bipyridine)ruthenium(II) Hexafluorophosphate, $[Ru(dmb)_3](PF_6)_2$. Yield: 76.5 mg (81%). Anal. Calcd for $C_{36}H_{36}F_{12}N_6P_2Ru$: C, 45.82; H, 3.84; N, 8.91. Found: C, 45.44; H, 4.01; N, 8.85. MS (ES): *m/z* 799 ($[M - PF_6]^+$, 100%), 327 ($[M - 2PF_6]^{2+}$, 76%).

(b) Tris(4,4′-diphenyl-2,2′-bipyridine)ruthenium(II) Hexafluorophosphate, $[Ru(dpb)_3](PF_6)_2$. Yield: 104 mg (79%). Anal. Calcd for $C_{66}H_{48}F_{12}N_6P_2Ru$: C, 60.23; H, 3.68; N, 6.39. Found: C, 60.00; H, 3.77; N, 6.29. MS (ES): *m/z* 1171.4 ($[M - PF_6]^+$, 43%), 513.3 ($[M - 2PF_6]^{2+}$, 100%).

(c) Tris(4,4′-di-*o*-tolyl-2,2′-bipyridine)ruthenium(II) Hexafluorophosphate, $[Ru(dotb)_3](PF_6)_2$. Yield: 105 mg (75%). Anal. Calcd for $C_{72}H_{60}F_{12}N_6P_2Ru$: C, 61.76; H, 4.32; N, 6.00. Found: C, 61.16; H, 4.82; N, 5.54. MS (ES): *m/z* 1255 ($[M - PF_6]^+$, 9%), 555 ($[M - 2PF_6]^{2+}$, 100%).

(d) Tris(4,4′-di-*p*-tolyl-2,2′-bipyridine)ruthenium(II) Hexafluorophosphate, $[Ru(dptb)_3](PF_6)_2$. Yield: 92 mg (66%). Anal. Calcd for $C_{72}H_{60}F_{12}N_6P_2Ru$: C, 61.76; H, 4.32; N, 6.00. Found: C, 61.28; H, 4.79; N, 5.66. MS (ES): *m/z* 1255 ($[M - PF_6]^+$, 1%), 555 ($[M - 2PF_6]^{2+}$, 100%).

(e) Tris(4,4′-di-mesityl-2,2′-bipyridine)ruthenium(II) Hexafluorophosphate, $[Ru(dmesb)_3](PF_6)_2$. Yield: 122 mg (78%). Anal. Calcd for $C_{84}H_{84}F_{12}N_6P_2Ru$: C, 64.32; H, 5.40; N, 5.36. Found: C, 63.84; H, 5.55; N, 5.50. MS (ES): *m/z* 1424 ($[M - PF_6]^+$, 4%), 639 ($[M - 2PF_6]^{2+}$, 100%).

(f) Bis(4,4′-dimethyl-2,2′-bipyridine)(4,4′-diphenyl-2,2′-bipyridine)-ruthenium(II) Hexafluorophosphate, $[Ru(dmb)_2(dpb)](PF_6)_2 \cdot C_7H_8$. This compound was prepared by a modified literature procedure[17] with $Ru(dmb)_2Cl_2$ and dpb. The $Ru(dmb)_2Cl_2$ starting material was made from $Ru(DMSO)_4Cl_2$[15] rather than $RuCl_3$. The crude product, a dark-orange-red solid, was chromatographed on alumina (20% CH_3CN/CH_2Cl_2) and recrystallized by evaporation of CH_3CN from toluene. Yield: 86%. Anal. Calcd for $C_{46}H_{40}F_{12}N_6P_2Ru \cdot C_7H_8$: C, 54.87; H, 4.17; N, 7.25. Found: C, 55.23; H, 4.47; N, 7.22.

Physical Measurements. Cyclic Voltammetry. Electrochemical measurements were carried out with a BAS 100A electrochemical analyzer. Solutions of the compounds were dissolved in distilled CH_3-

(11) Willner, I.; Willner, B. *Adv. Photochem.* **1995**, *20*, 217.
(12) Scandola, F.; Bignozzi, C. A.; Indelli, M. T. *Photosensitization and Photocatalysis Using Inorganic and Organometallic Compounds*; Kluwer Academic: Dordrecht, The Netherlands, 1993.
(13) Juris, A.; Baragelletti, S.; Campagna, S.; Balzani, V.; Belser, P.; von Zelewski, A. *Coord. Chem. Rev.* **1988**, *84*, 85.
(14) Damrauer, N. H.; Cerullo, G.; Yeh, A.; Boussie, T. R.; Shank, C. V.; McCusker, J. K. *Science* **1997**, *275*, 54.
(15) Evans, I. P.; Spencer, A.; Wilkinson, G. *J. Chem. Soc., Dalton Trans.* **1973**, 204−209.
(16) Maerker, G.; Case, F. C. *J. Am. Chem. Soc.* **1958**, *80*, 2745.
(17) Mabrouk, P. A.; Wrighton, M. S. *Inorg. Chem.* **1986**, *25*, 526.

CN containing NBu_4PF_6 (ca. 0.1 M) as the supporting electrolyte. A standard three-electrode setup was used with a glassy carbon working electrode, Pt wire counter electrode, and a $Ag/Ag(NO_3)$ electrode as the reference. All measurements were made inside an Ar-filled glovebox. On the basis of the large peak-to-peak separation obtained on the ferrocene standard ($\Delta E_p > 90$ mV), an IR compensation was applied that resulted in a more reasonable splitting of $\Delta E_p = 65$ mV for ferrocene; this correction was therefore applied to data collected on the ruthenium complexes. It should be noted that while the IR compensation brought ΔE_p values much closer to the theoretical value of 59 mV, $E_{1/2}$ values were not significantly affected. With the exception of $[Ru(dptb)_3](PF_6)_2$, the $Ru^{II/III}$ oxidative wave and all three $bpy^{0/-}$ reductive waves showed reversible behavior over several successive scans for all of the molecules studied. In addition, no dependence of the data on scan rate over a range of 50−500 mV s^{-1} was discernible. In the case of $[Ru(dptb)_3](PF_6)_2$, the oxidative wave was unremarkable. However, scans beyond the first reductive wave showed irreversible behavior. A coating was observed to form on the electrode, suggesting that the complex was depositing on the surface of the electrode. Thus, cathodic data for $[Ru(dptb)_3](PF_6)_2$ were limited to one-electron reduction of the complex.

Static Absorption and Emission Spectra. All spectroscopic data were obtained on samples dissolved in spectral- or HPLC-grade solvents. Absorption spectra were measured with a Hewlett-Packard HP8452A diode array spectrophotometer. Each spectrum corresponds to a signal-average of 20 individual spectra collected at 0.1-s intervals. Absorption maxima are accurate to ±2 nm.

Emission spectra were collected by using an Instruments SA/Jobin Yvon-Spex Fluoromax photon-counting fluorimeter equipped with a Xe arc lamp excitation source and a Hamamatsu R928P photomultiplier tube operating at −900 Vdc. Data were obtained on thoroughly deoxygenated solutions of each complex having an optical density of ca. 0.1 (1 cm path length) at the excitation wavelength. Background measurements on the solvent blanks revealed no signals other than the expected Raman lines of the neat solvent. Excitation spectra in the region of the $^1MLCT \leftarrow {}^1A_1$ visible absorption band ($\lambda > 400$ nm), corrected for the Xe lamp spectral profile, matched the ground-state absorption spectrum for each of the Ru complexes studied; all spectral and quantum yield measurements were therefore carried out at a single excitation wavelength (450 nm). The resolution of each spectrum is estimated to be ±2 nm based on the RLD of the emission monochromator and the slit setting of the instrument. Spectra were corrected for instrument response by using a NIST standard of spectral irradiance (Optronic Laboratories, Inc., OL220M tungsten quartz lamp). All subsequent data manipulations were carried out with the corrected spectra.

Radiative quantum yield (Φ_r) measurements were made on optically thin solutions (OD ≈ 0.1) thermostated at 298 ± 1 K with a Fisher Model 9105 circulating bath. Values are reported relative to $[Ru(bpy)_3](PF_6)_2$ in CH_3CN ($\Phi_r = 0.062$)[18] and calculated according to the following equation,[19]

$$\Phi_{unk} = \Phi_{std}\left(\frac{I_{unk}}{A_{unk}}\right)\left(\frac{A_{std}}{I_{std}}\right)\left(\frac{\eta_{unk}}{\eta_{std}}\right)^2 \quad (2)$$

where Φ_{unk} is the radiative quantum yield of the sample, Φ_{std} is the radiative quantum yield of the standard, I_{unk} and I_{std} are the integrated emission intensities of the sample and standard, respectively, A_{unk} and A_{std} are the absorbances of the sample and standard, respectively, at the excitation wavelength (450 nm), and η_{unk} and η_{std} are the indexes of refraction of the sample and standard solutions. For the latter, values of η corresponding to the pure solvent have been assumed. Multiple measurements on each sample indicated a precision of ca. 8% for our reported values of Φ_r. This is given as the relative uncertainty in Table 2 (vide infra) and is representative of 2σ for these measurements. The absolute accuracy is estimated to be on the order of 10% on the basis of the original reference for the standard.

Emission spectra were fit with a program developed at the University of North Carolina at Chapel Hill.[20] In converting the wavelength data into energy units, the correction of Parker and Rees was applied.[21] Fitting of the spectra involves multiparameter minimization of a nonlinear equation (eq 5, vide infra). As such, several regions of parameter space for all of the variables were explored. The values reported herein are believed to correspond to the global minimum in each case. The best fit was determined by visual inspection as well as minimization of the root-mean-square deviation.

Nanosecond Time-Resolved Emission and Absorption. Time-resolved measurements on the nanosecond time scale were carried out with an optical parametric oscillator-based spectrometer configured as follows. The third harmonic of a Spectra-Physics Model GCR-150−10 (ca. 130 mJ at 354.7 nm, nominal pulse width of 7 ns) is directed into an Opotek, Inc. Magic Prism. Parametric generation of the signal pulse, λ_s, affords excitation wavelengths in the 420−680 nm range with a pulse width of ca. 5 ns fwhm. For time-resolved emission, this pulse is focused into a 1 mm bore fiber optic filament (Thor Labs). The output of the fiber is collimated and soft-focused through the sample with the excitation energy attenuated to ∼100 μJ/pulse, typically, using neutral density filters. The emitted light is collected at 90° to the excitation via matched back-to-back plano-convex lenses ($f_o = 200$ mm, $\phi = 90$ mm) and coupled into a McPherson Model 272 200 mm *f*/2 monochromator equipped with a 100 mm diameter holographic grating (1140 G/mm). Typical slit settings are 0.5 mm for both the entrance and exit slits. Detection is achieved by using a negatively-biased Hamamatsu R928 photomultiplier tube operated at a voltage of −650 Vdc. The tube is housed in a RF and magnetically shielded PMT housing (Thorn EMI Electron Tubes). The PMT signal is terminated through a 50 Ω resistor to a LeCroy Model 9360 Digitizing Oscilloscope. Linearity of the PMT signal is checked, using neutral density filters, with the signal intensity adjusted if necessary via attenuation of the excitation beam. The data from the scope, representing a 200-shot signal average collected at a repetition rate of 10 Hz, is transferred to a computer and processed by using programs of local origin.

The time-resolved absorption measurements use the output from the OPO directly (i.e., no fiber optic). The beam is cylindrically focused onto the sample at 90° to the probe beam. Excitation energies used are typically in the range of 1−3 mJ/pulse. The probe consists of a current-intensified pulsed Xe arc lamp (Applied Photophysics, Ltd.). The white light is passed through a cylindrical quartz container filled with the solvent in which the sample is dissolved to remove IR radiation. The beam is then focused through a series of matched achromatic lenses and passed through the sample such that the probe is effectively collimated through the 1 cm path length of the cell, matching the spatial profile of the pump. A second set of matched achromats and an aplanatic meniscus lens couples the probe beam into a Jarrel-Ashe Monospec 18 monochromator. Detection is achieved by using a negatively-biased Hamamatsu R446 photomultiplier tube operating at −600 Vdc and housed in a Products for Research PMT housing. To compensate for the high photon flux of the probe beam, we modified the standard circuit of the R446 so as to only use the first five dynode stages of the tube. This results in better linearity of the tube response at high input intensity, improving the useful dynamic range of the tube for this type of experiment. As with the emission experiment, the signal from the R446 is terminated through a 50 Ω resistor to the LeCroy scope. The entire experiment is synchronized by using a timing circuit of local design. The data, consisting of a 20-shot average of both the signal and the baseline at a repetition rate of 1 Hz, is transferred to a computer for analysis with programs of local origin.

Raman Spectroscopy. Ground-state resonance Raman spectra were acquired with 441.6 nm excitation by using a HeCd (Liconix 4240) laser. The scattered radiation was collected in a 135° backscattering geometry from samples (mM in complex) in NMR tubes and dispersed through a Spex 1877 Triplemate Spectrometer equipped with a 1200 G/mm grating. The detection system consists of a Princeton Instruments Intensified Charge Coupled Device (ICCD) detector interfaced to a ST130 controller. Calibration of the ICCD was performed routinely by running the Raman spectra of neat solvents (cyclohexane and

(18) Casper, J. V.; Meyer, T. J. *J. Am. Chem. Soc.* **1983**, *105*, 5583−5590.

(19) Demas, J. N.; Crosby, G. A. *J. Phys. Chem.* **1971**, *75*, 991−1024.

(20) Claude, J. P. Photophysics of Polypyridyl Complexes of Ruthenium(II), Osmium(II), and Rhenium(I). Ph.D. Thesis, University of North Carolina at Chapel Hill, 1995; p 191.

(21) Parker, C. A.; Rees, W. T. *Analyst (London)* **1960**, *85*, 587.

Table 1. Crystallographic Data for $[Ru(dmesb)_3](PF_6)_2$ and $[Ru(dmb)_2(dpb)](PF_6)_2 \cdot C_7H_8$

	$[Ru(dmesb)_3](PF_6)_2$	$[Ru(dmb)_2(dpb)](PF_6)_2 \cdot C_7H_8$
empirical formula	$RuP_2F_{12}N_6C_{84}H_{84}$	$RuP_2F_{12}N_6C_{53}H_{42}$
formula weight	1568.85	1153.95
crystal color, habit	orange, plate	red, thin blades
crystal system	triclinic	monoclinic
space group	$P\bar{1}$ (no. 2)	$P2_1/a$ (no. 14)
temp (K)	176 ± 1	128 ± 2
cell dimensions		
a(Å)	12.3272(1)	21.1765(3)
b (Å)	15.6454(1)	11.7372(2)
c (Å)	22.0431(2)	21.3953(3)
α (deg)	107.102(1)	90.000
β (deg)	101.909(1)	109.575(1)
γ (deg)	98.903(1)	90.000
V (Å^3)	6868.94(8)	5010.5(1)
Z	2	4
goodness of fit (S)[a]	2.42	2.06
R[b]	0.068	0.064
R_w[c]	0.078	0.069

[a] $S = [\sum w(|F_o| - |F_c|)^2/(m-n)]^{1/2}$. [b] $R = \sum||F_o| - |F_c||/\sum|F_o|$. [c] $R_w = [\sum w(|F_o| - |F_c|)^2/\sum w|F_o|^2]^{1/2}$.

benzene) which have known vibrational peaks in the region of interest. The final spectra were a result of a total integration time of 3 min with laser power at the sample of 30 mW.

Excited-state spectra were acquired with the third harmonic (354.7 nm) of a Quanta-Ray DCR-2A pulsed Nd:YAG laser operating at 10 Hz. Q-switched laser pulses (7ns) were used to both create the excited state and serve as a source for the Raman scattering. The scattered radiation was collected in a 135° backscattering geometry from a degassed sample (1 mM in complex) in a spinning NMR tube into a Spex 1877 Triplemate spectrometer equipped with a grating of 1800 G/mm. The detection system consists of a Princeton Instruments Intensified Charge Coupled Device detector operating in the gated mode with a ST 130 controller. Timing was controlled by a Princeton Instruments FG-100 pulse generator. The final spectra were a result of a total integration time of 6 min with laser power at the sample of 3−5 mJ/pulse. In no case, for any of the photophysical measurements, was there evidence of photodegradation of the sample.

X-ray Structure Determinations. Single-crystal X-ray structure determinations of $[Ru(dmesb)_3](PF_6)_2$ and $[Ru(dmb)_2(dpb)](PF_6)_2 \cdot C_7H_8$ were both carried out in the CHEXRAY facility of the University of California at Berkeley by Dr. Fred Hollander.

(a) $[Ru(dmesb)_3](PF_6)_2$. Orange plate-like crystals of $[Ru(dmesb)_3](PF_6)_2$ were obtained by diffusion of pentane into a 1:1 THF/toluene solution of the compound. One crystal having approximate dimensions of 0.40 × 0.15 × 0.04 mm was mounted on a glass fiber. All measurements were made on a Siemens SMART[22] diffractometer with graphite monochromated Mo Kα radiation. Crystallographic data are summarized in Table 1. Cell constants and an orientation matrix obtained from a least-squares refinement using the measured positions of 8192 reflections with $I > 10\sigma$ in the range $3.00 < 2\theta < 45.00°$ corresponded to a primitive triclinic cell. On the basis of a statistical analysis of the intensity distribution and the successful solution and refinement of the structure, the space group was determined to be $P\bar{1}$. Data were integrated to a maximum 2θ value of 46.5°. The data were corrected for Lorentz and polarization effects. No decay correction was applied. An empirical absorption correction based on a comparison of redundant and equivalent data and an ellipsoidal model of the absorption surface was applied by using XPREP[23] ($T_{max} = 0.99$, $T_{min} = 0.83$). The 18989 integrated and corrected reflections were averaged to yield 10918 unique data ($R_{int} = 0.047$). The structure was solved by direct methods[24] and expanded by using Fourier techniques.[25] All non-hydrogen atoms were refined anisotropically. Hydrogen atoms were included at calculated positions but not refined. The final cycle of full-matrix least-squares refinement was based on 8182 observed reflections ($I > 3.00\sigma(I)$) and 949 variable parameters and converged (largest parameter shift was 0.02 times its esd) with unweighted and weighted agreement factors of $R = 0.068$ and $R_w = 0.078$. The standard deviation of an observation of unit weight was 2.42. The weighting scheme was based on counting statistics and included a factor ($p = 0.030$) to downweight the intense reflections. Plots of $\sum w(|F_o| - |F_c|)^2$ versus $|F_o|$, reflection order in data collection, $\sin(\theta/\lambda)$, and various classes of indices showed no unusual trends. All calculations were performed with the teXsan[26] crystallographic software package of Molecular Structure Corporation.

After refinement of all atoms in the molecule, the two largest residual electron density peaks (1.12 and 1.00 e$^-$/Å^3) were located near bpy nitrogens N3 and N4, while the remaining residuals were significantly smaller (0.65 e$^-$/Å^3 or less). Closer inspection of the Ru−N bond distances revealed that the Ru−N3 and Ru−N4 bonds were approximately 0.03 Å longer than the other four Ru−N bonds. Initially it was thought that these two peaks might have resulted from disorder between $[Ru(dmesb)_3]^{2+}$ cations and an impurity of $Ru(dmesb)_2Cl_2$ co-crystallized in the lattice. Refinement of such a model indicated 5.7% dichloride impurity. However, analytical measurements of the same sample from which the present crystal was selected did not reveal any such impurity. In addition, the resulting Ru−Cl bond distances of 2.8−2.9 Å are much longer than the 2.408 Å average obtained from the Cambridge Structural Database, and the Cl−Ru−Cl angle of 68° was also unreasonable. No satisfactory chemical or crystallographic explanation has been proposed to account for these peaks, but we do not believe the problem is significant for the structural features in which we are interested.

(b) $[Ru(dmb)_2(dpb)](PF_6)_2 \cdot C_7H_8$. Thin red crystals of $RuP_2F_{12}N_6C_{53}H_{42}$ were obtained by evaporation of CH_3CN from a toluene solution of the compound. A fragment of one of these crystals having approximate dimensions of 0.23 × 0.35 × 0.03 mm was mounted on a glass fiber with Paratone N hydrocarbon oil. Crystallographic data are summarized in Table 1. Cell constants and an orientation matrix obtained from a least-squares refinement using the measured positions of 7948 reflections with $I > 10\sigma$ in the range $3.00 < 2\theta < 45.00°$ corresponded to a primitive monoclinic cell. The systematic absences of h01 ($h \neq 2n$) and 0k0 ($k \neq 2n$) uniquely determine the space group to be $P2_1/a$. Data were integrated to a maximum 2θ value of 51.5°. The data were corrected for Lorentz and polarization effects. No decay correction was applied. Analysis of redundant and equivalent reflections indicated that an empirical absorption correction was justified, and an ellipsoidal correction was applied ($T_{max} = 0.98$, $T_{min} = 0.83$). The 23012 reflections were averaged to yield 9076 unique reflections ($R_{int} = 0.078$). The structure was solved by direct methods[27] and expanded by using Fourier techniques. All non-hydrogen atoms except the methyl carbon on the toluene of solvation were refined anisotropically. Hydrogen atoms were included at calculated positions but not refined. The final cycle of full-matrix least-squares refinement was based on 5065 observed reflections ($I > 3.00\sigma(I)$) and 662 variable parameters and converged (largest parameter shift was 0.02 times its esd) with unweighted and weighted agreement factors of $R = 0.064$ and $R_w = 0.069$. The standard deviation of an observation of unit weight was 2.06. The weighting scheme was based on counting statistics and included a factor ($p = 0.035$) to downweight the intense reflections. The maximum and minimum peaks on the final difference Fourier map corresponded to 0.64 and −0.86 e$^-$/Å^3, respectively.

Calculations. Ab initio calculations were carried out with the Gaussian 92 suite of programs.[28] The molecular geometry for neutral 4-phenylpyridine (C_2) was fully optimized using restricted

(22) SMART Area-Detector Software Package; Siemens Industrial Automation, Inc.: Madison, WI, 1995.

(23) XPREP (v 5.03), Part of the SHELXTL Crystal Structure Determination Package; Siemens Industrial Automation, Inc.: Madison, WI, 1995.

(24) Altomare, A.; Burla, M. C.; Cascarano, G.; Giacovazzo, C.; Guagliardi, A.; Moliterni, A. G. G.; Polidori, G. *J. Appl. Crystallogr.* **1996**, *29*, 341.

(25) *DIRDIF92*; Beurskens, P. T.; Admiraal, G.; Beurskens, G.; Bosman, W. P.; Garcia-Granda, S.; Gould, R. O.; Smits, J. M. M.; Smykalla, C. The DIRDIF program system, Technical Report of the Crystallography Laboratory, University of Nijmegen, The Netherlands, 1992.

(26) *teXsan*: Crystal Structure Analysis Package, Molecular Structure Corporation, 1985 & 1992.

(27) *SAPI91*: Fan Hai-Fu, 1991. Structure Analysis Programs with Intelligent Control, Rigaku Corporation, Tokyo, Japan.

Hartree−Fock (RHF)-calculations as well as second order perturbation theory (MP2). The basis sets used were 3-21G(d) and 6-31G(d). In addition, the energy and geometry of the two transition states corresponding to coplanar ring systems (C_{2v}, $\theta = 0°$) and perpendicular ring systems (C_{2v}, $\theta = 90°$) were calculated with the above methods and basis sets. Here, θ is the dihedral angle between the pyridyl-containing and phenyl-containing planes. In these calculations, only this dihedral angle was locked. For all stationary points determined by RHF methods, the analytic Hessian was calculated and diagonalized to determine whether the structures are minima or transition states. Stationary states showed only positive definite vibrational modes while transition states had one vibrational mode with an imaginary frequency. The molecular geometry for the radical anion (4-phenylpyridine)$^-$ was fully optimized by using open-shell unrestricted Hartree−Fock (UHF) calculations with inclusion of diffuse functions in the basis set (3-21+G(d) and 6-31+G(d)). The analytic Hessian was calculated and diagonalized, showing that the coplanar ($\theta = 0°$) structure was a stationary minimum (only positive definite vibrational modes). A MP2 zero-point energy calculation was performed on the anion with use of a fixed geometry optimized at UHF/6-31+G(d). Finally, calculations were made to estimate the energetic driving force for forming the coplanar anion structure from a canted "Franck−Condon" state ($\theta = 44.6°$; this dihedral angle was taken from the MP2/6-31G(d) full optimization of the neutral). The energy and geometry of this nonstationary state of the anion was calculated at UHF/3-21+G(d) and UHF/6-31+G(d) by fixing $\theta = 44.6°$ but allowing other variables to optimize (within the overall imposed C_2 symmetry). A MP2 zero-point energy calculation of this nonstationary state was performed by using the geometry determined at UHF/6-31+G(d).

Results and Discussion

I. The Photophysical Properties of $[Ru(dmb)_3](PF_6)_2$ versus $[Ru(dpb)_3](PF_6)_2$: Evidence for Intraligand Excited-State Delocalization. Our initial interest in $[Ru(dpb)_3](PF_6)_2$ was sparked by its anomalously high radiative quantum yield, reported to be on the order of 30%.[29,30] This is almost a factor of five larger than that of $[Ru(bpy)_3](PF_6)_2$ and suggests a profound influence of the dpb ligand on the photophysics of the compound. Surprisingly, there is very little information in the literature about this molecule despite its remarkable emissive properties. Watts and Crosby[31] reported on the photophysical properties of the compound and suggested an explanation for its unusually large Φ_r based on changes in spin−orbit coupling and excited-state mixing. The compound has appeared in the context of other studies,[32−38] but nothing that further details its photophysics. We decided to reexamine the photophysical properties of the compound in an effort to understand the microscopic origin of its high quantum yield for emission.

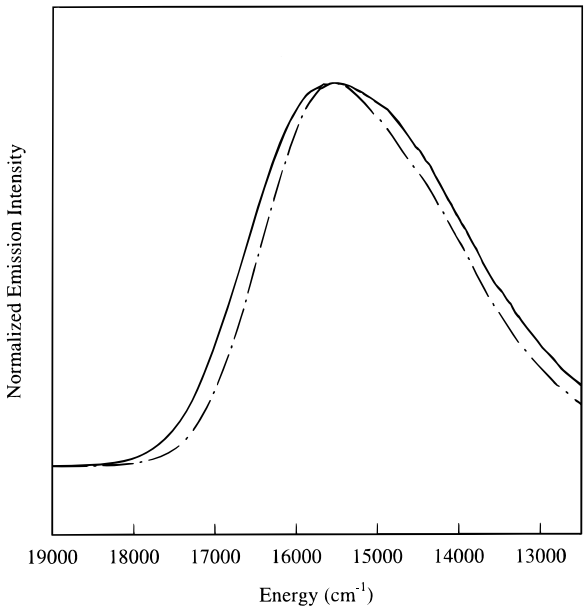

Figure 1. Emission spectra of $[Ru(dmb)_3](PF_6)_2$ (solid line) and $[Ru(dpb)_3](PF_6)_2$ (dashed line) in deoxygenated CH_3CN solution at 298 K.

For comparative purposes we carried out parallel measurements on $[Ru(dmb)_3](PF_6)_2$. The emission spectra for both $[Ru(dmb)_3](PF_6)_2$ and $[Ru(dpb)_3](PF_6)_2$ in CH_3CN at 298 K are shown in Figure 1. Qualitatively, it can be seen that the emission in $[Ru(dpb)_3]^{2+}$ presents a narrower spectral profile as compared to $[Ru(dmb)_3]^{2+}$. The radiative quantum yields as well as results from time-resolved emission measurements on these two compounds are given in Table 2. Consistent with the reports in the literature, we measure a significantly larger value of Φ_r for $[Ru(dpb)_3]^{2+}$ relative to both $[Ru(dmb)_3]^{2+}$ and $[Ru(bpy)_3]^{2+}$, although we find a slightly smaller value for Φ_r than previously reported. Examination of the radiative and nonradiative decay rate constants, derived from the observed lifetime and quantum yield, reveals that the increase in Φ_r for $[Ru(dpb)_3]^{2+}$ is due to both an increase in k_r and a decrease in k_{nr}. Again, this is consistent with data reported by Watts and Crosby.[31] Our results indicate that the change in k_r is on the order of 60%, while the change from 1.06×10^6 to 5.0×10^5 s^{-1} represents a decrease of more than a factor of 2 in the nonradiative decay rate for $[Ru(dpb)_3]^{2+}$ relative to $[Ru(dmb)_3]^{2+}$. These experimental observations can be explained within the context of a model that we have developed and are a direct consequence, we believe, of excited-state intraligand delocalization in $[Ru(dpb)_3]^{2+}$.

The Drop in k_{nr}: Considerations of the Energy Gap Law. It has been found that, in general, the behavior of most transition metal systems can be accommodated by the so-called energy gap law.[8,39,40] This model, which closely resembles in physical construct the multiphonon nonadiabatic descriptions of electron transfer developed by Bixon, Jortner, and others,[41−46] describes a nonradiative transition in terms of a coupling of vibronic states on an initial potential energy surface to isoenergetic levels of

(28) Frisch, M. J.; Trucks, G. W.; Head-Gordon, M.; Gill, P. M. W.; Wong, M. W.; Foresman, J. B.; Johnson, B. G.; Schlegel, H. B.; Robb, M. A.; Replogle, E. S.; Gomperts, R.; Andres, J. L.; Raghavachari, K.; Binkley, J. S.; Gonzalez, C.; Martin, R. L.; Fox, D. J.; Defrees, D. J.; Baker, J.; Stewart, J. J. P.; Pople, J. A. GAUSSIAN 92, Revision G.2; Gaussian, Inc.: Pittsburgh, PA, 1992.
(29) Cook, M. J.; Lewis, A. P.; McAuliffe, G. S. G.; Skarda, V.; Thomson, A. J.; Glasper, J. L.; Robbins, D. J. *J. Chem. Soc., Perkin Trans. 2* **1984**, 1293.
(30) Cook, M. J.; Thomson, A. J. *Chem. Br.* **1984**, 914.
(31) Watts, R. J.; Crosby, G. A. *J. Am. Chem. Soc.* **1972**, *94*, 2606.
(32) Watts, R. J.; Crosby, G. A. *J. Am. Chem. Soc.* **1971**, *93*, 3184.
(33) Harrigan, R. W.; Crosby, G. A. *J. Phys. Chem.* **1973**, *59*, 3468.
(34) Lin, C. T.; Boettcher, W.; Chou, M.; Creutz, C.; Sutin, N. *J. Am. Chem. Soc.* **1976**, *98*, 6536.
(35) Ohsawa, Y.; Hanck, K. W.; DeArmond, M. K. *J. Electroanal. Chem.* **1984**, *175*, 229.
(36) Pande, I. M.; Siddiqui, A. *Modell., Meas. Control, C* **1993**, *39*, 7.
(37) Skarda, V.; Cook, M. J.; Lewis, A. P.; McAuliffe, G. S. G.; Thompson, A. J.; Robbins, D. J. *J. Chem. Soc., Perkin Trans. 2* **1984**, *8*, 1309.
(38) Cook, M. J.; Lewis, A. P.; McAuliffe, G. S. G.; Skarda, V.; Thompson, A. J.; Glasper, J. L.; Robbins, D. J. *J. Chem. Soc., Perkin Trans. 2* **1984**, *8*, 1303.
(39) Barqawi, K. R.; Murtaza, Z.; Meyer, T. J. *J. Phys. Chem.* **1991**, *95*, 47.
(40) Casper, J. V.; Meyer, T. J. *J. Phys. Chem.* **1983**, *87*, 952.
(41) Freed, K. F.; Jortner, J. *J. Chem. Phys.* **1970**, *62*, 72.
(42) Englman, R.; Jortner, J. *Mol. Phys.* **1970**, *18*, 145.
(43) Jortner, J. *J. Chem. Phys.* **1976**, *64*, 4860.
(44) Hopfield, J. *Proc. Natl. Acad. Sci. U.S.A.* **1974**, *71*, 3640.
(45) Jortner, J.; Bixon, M. *Ber. Bunsen-Ges. Phys. Chem.* **1995**, *99*, 296.
(46) Buhks, E.; Navon, G.; Bixon, M.; Jortner, J. *J. Am. Chem. Soc.* **1980**, *102*, 2918.

Table 2. Room Temperature Excited State Emission Properties of the dpb Series in CH_3CN

complex	$\lambda_{em\ max}$ (nm)	τ (μs)[a]	ϕ_{em}[b]	k_r (10^5 s^{-1})	k_{nr} (10^5 s^{-1})
$[Ru(dmb)_3](PF_6)_2$	632	0.875 ± 0.03	0.073 ± 0.006	0.83 ± 0.09	10.6 ± 1
$[Ru(dmesb)_3](PF_6)_2$	628	0.94 ± 0.03	0.099 ± 0.008	1.05 ± 0.1	9.6 ± 1
$[Ru(dotb)_3](PF_6)_2$	628	1.36 ± 0.04	0.16 ± 0.01	1.16 ± 0.1	6.2 ± 0.9
$[Ru(dptb)_3](PF_6)_2$	640	1.52 ± 0.05	0.20 ± 0.02	1.32 ± 0.1	5.2 ± 0.7
$[Ru(dpb)_3](PF_6)_2$	638	1.60 ± 0.05	0.20 ± 0.02	1.25 ± 0.1	5.0 ± 0.7

[a] Relative uncertainty in lifetime measurement, reported here as 2σ, does not exceed 4%. [b] Error bars represent reproducibility within 2σ, which includes the uncertainty in the measurement of the standard.

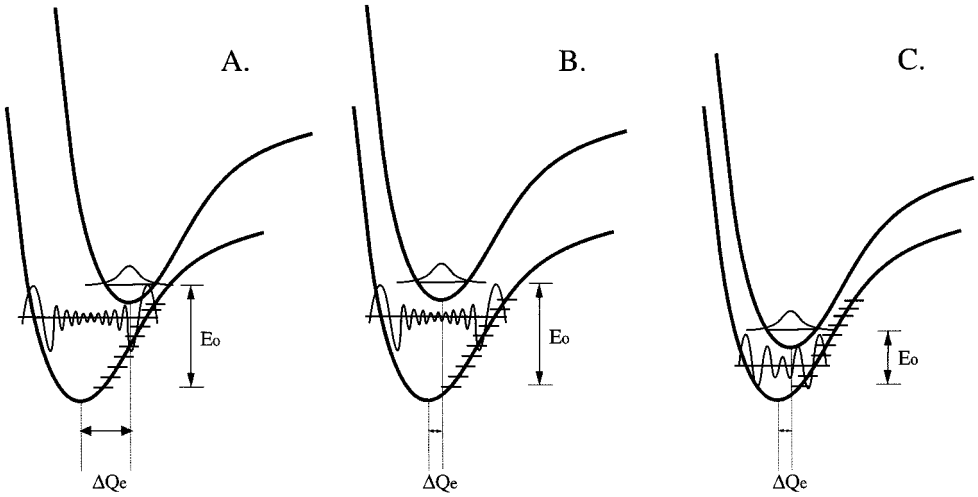

Figure 2. Graphical illustration of the factors influencing vibrational overlap for non-radiative excited-state decay. Starting from nominal values of the energy gap (E_0) and relative nuclear displacement (ΔQ_e) in B, the energy gap law predicts that changes in non-radiative decay rates can be linked to changes in the energy gap (C) as well as changes in the degree of excited-state distortion relative to the ground state along specified nuclear coordinate(s) (A).

the final state. For the purposes of this discussion, we can consider the energy gap law in a simplified form as given in eq 3,[8,47]

$$k_{nr} \propto \exp\left(\frac{-\gamma E_0}{\hbar\omega_M}\right) \qquad \gamma = \ln\left(\frac{E_0}{S_M \hbar\omega_M}\right) - 1 \tag{3}$$

where the energy gap E_0 is related to the zero-point energy (ZPE) separation of the two coupled surfaces. The $\hbar\omega_M$ term describes, in the limit of a single configurational coordinate model, the average energy of the vibrational mode(s) that couples the final state to the initial state. The degree to which the two surfaces are vibronically coupled is gauged by the Huang−Rhys factor S_M,

$$S_M = \frac{1}{2}\left(\frac{M\omega_M}{\hbar}\right)(\Delta Q_e)^2 \tag{4}$$

where M is the reduced mass of the oscillator, ω_M is the fundamental frequency, and ΔQ_e represents the difference between the ground- and excited-state equilibrium geometries with respect to the specified nuclear (i.e., vibrational) coordinate. The effect changes in both E_0 and ΔQ_e have on vibrational overlap (and therefore k_{nr}) is shown pictorially in Figure 2. Starting with the central potential energy surface diagram (B), a decrease in the energy gap at constant ΔQ_e (C) results in an increase in the vibrational overlap between the lowest energy vibrational state(s) of the excited-state surface and isoenergetic vibrational states of the ground-state surface. Conversely, increasing the energy gap has the opposite effect, with the concomitant decrease in vibrational overlap leading to a smaller value for k_{nr}. Changes in the degree of displacement between the excited-state and ground-state potential energy surfaces have similar consequences, with a larger ΔQ_e (A), favoring vibrational overlap and leading to a larger value for k_{nr}. To ascertain to what extent either or both of these factors are influencing the properties of $[Ru(dpb)_3](PF_6)_2$, we must examine each in detail.

The Role of ΔQ_e. It is evident from Figure 1 that the emission spectrum of $[Ru(dpb)_3](PF_6)_2$ is more narrow than that of $[Ru(dmb)_3](PF_6)_2$. This observation, along with their similar emission maxima (Table 2), suggests that the excited-state and ground-state potential energy surfaces are more nested in $[Ru(dpb)_3](PF_6)_2$ than in $[Ru(dmb)_3](PF_6)_2$. This can be quantified by fitting the emission spectra of these molecules. This type of analysis, which has been described in detail elsewhere,[20,48] basically consists of modeling the emission spectrum as a summation of individual emission envelopes corresponding to each of the various radiative (i.e., vertical) transitions that are possible between the excited state and the ground state. The intensities of these components are determined by the Franck−Condon factors, i.e., the magnitude of the overlap between the vibrational wave functions of the excited state and the ground state. The details of the fit of an emission spectrum are therefore going to be a function of the nature of the vibrational modes that are coupled to the transition (e.g., $\hbar\omega_M$), the relative vertical and horizontal positions of the excited-state and ground-state potential energy surfaces (E_0 and S_M, respectively), and effects due to the surrounding medium. This model can in principal accommodate all $3N - 6$ modes of the molecule plus contributions from the solvent. For coupling to a single vibrational mode $\hbar\omega_M$,[49] the emission intensity at a given energy $\bar{\nu}$, $I(\bar{\nu})$, can be described by eq 5,

(47) The electronic coupling between the two multielectronic states is described by an additional term β, not indicated in eq 4. For the purposes of this discussion, we have assumed that this term is constant.

(48) Claude, J. P.; Meyer, T. J. *J. Phys. Chem.* **1995**, *99*, 51.

$$I(\bar{\nu}) = \sum_{\upsilon_M=0}^{n} \left\{ \left(\frac{E_0 - \upsilon_M \hbar\omega_M}{E_0} \right)^3 \left(\frac{S_M^{\upsilon_M}}{\upsilon_M!} \right) \times \exp\left[-4 \ln(2) \left(\frac{\bar{\nu} - E_0 + \upsilon_M \hbar\omega_M}{\Delta\bar{\nu}_{0,1/2}} \right)^2 \right] \right\} \quad (5)$$

where $\hbar\omega_M$, E_0, and S_M are as defined above, and $\Delta\nu_{0,1/2}$ is the homogeneously broadened band width of the zeroth-order vibronic transition (i.e., $\upsilon^* = 0 \rightarrow \upsilon = 0$). The index υ_M runs over the number of vibrational levels of $\hbar\omega_M$ in the ground state that serve as the final vibronic states. In fitting the spectra, it was necessary to include only three overtones of the ground vibrational level to adequately fit each spectrum.

Results of these analyses are given in Table 3 while a representative example of such a fit is illustrated in Figure 3. The important parameter from the fits of the spectra, as pertains to the present discussion, is the value of S_M. It can be seen from Table 3 that there is a 20% drop in S_M from $[Ru(dmb)_3](PF_6)_2$ (1.05) to $[Ru(dpb)_3](PF_6)_2$ (0.840). This change in the Huang−Rhys factor originates from differences in ΔQ_e between the two complexes via eq 4 and is therefore directly related to changes in the equilibrium geometries of the excited states of the compounds.

Assuming that the nature of the relevant nuclear coordinate is similar for both complexes[50] a smaller value of S_M indicates a smaller degree of excited-state distortion relative to the ground state along coordinates coupled to the $^3MLCT \rightarrow {}^1A_1$ relaxation. Since neither the room temperature fluid solution nor low-temperature glass spectra of these types of compounds typically exhibit sufficient structure to make a fit to more than two modes analytically reasonable, the "observed" frequency obtained from spectral fitting is best interpreted as a weighted average of all modes that contribute to excited-state decay. The ca. 1300 cm^{-1} frequency needed to fit our data therefore suggests a dominance of ring stretch modes in defining the potential energy surfaces most relevant for $^3MLCT \rightarrow {}^1A_1$ relaxation; this is a well-accepted notion in the literature.[51] Given this, the relative values of S_M we have found indicate that the magnitude of excited-state distortion along the ring stretching coordinates is smaller, on average, in $[Ru(dpb)_3](PF_6)_2$ than in $[Ru(dmb)_3](PF_6)_2$.

Energy Gap. To determine the extent to which ΔQ_e is causing the differences in the photophysical properties between these molecules, it is important to establish whether or not changes in E_0 might be contributing to the observed trends in k_{nr}. To do this, we can use the results from the spectral fitting discussed above.

Two different measures of the energy gap are afforded by the spectral fitting analysis; these values are given in Table 3. E_0 corresponds to the energy gap as determined solely by the displaced vibrational coordinates used to calculate the Franck−Condon factors (i.e., $\hbar\omega_M$), whereas E_{00} includes the effects of the low-frequency intramolecular and solvent modes that are treated classically in the current model. It can be seen that it makes little difference whether E_0 or E_{00} is used as a gauge: both parameters indicate that the $^3MLCT/^1A_1$ energy gap in $[Ru(dpb)_3](PF_6)_2$ is approximately 200−300 cm^{-1} smaller than in $[Ru(dmb)_3](PF_6)_2$. This result would argue for a larger value of k_{nr} for $[Ru(dpb)_3](PF_6)_2$ relative to $[Ru(dmb)_3](PF_6)_2$, in clear contradiction to the experimental observations.

Given that the excited state of interest effectively corresponds to an intramolecular redox reaction, we can also use the electrochemical properties of the molecule as a measure of the energy gap.[52] Electrochemical data for $[Ru(dmb)_3](PF_6)_2$ and $[Ru(dpb)_3](PF_6)_2$ in CH_3CN are listed in Table 4. Both complexes showed reversible electrochemistry for the first oxidative wave of the metal and all three reductive waves of the ligands. Estimated values for the energy gap of both compounds were calculated[53] and are also listed in Table 4. We note that changing from a methyl group to a phenyl group significantly affects the potentials of the individual redox pairs. The differences in redox potentials can be understood quite readily based on a comparison with work by Furue and co-workers.[54] These authors have looked at the electrochemistry of CF_3-substituted bipyridyl Ru^{II} complexes, and they report values for the oxidation of $[Ru(bpy)_3](PF_6)_2$ and $[Ru(4,4'\text{-BTFMB})_3](PF_6)_2$ (4,4′-BTFMB = 4,4′-bis(trifluoromethyl)-2,2-bipyridine) in CH_3CN of +1.27 and +1.75 V versus SCE, respectively. The 480 mV increase in the $Ru^{II/III}$ couple was attributed to the strong σ-withdrawing properties of the CF_3 substituents. Phenyl groups are considered to be electron withdrawing, albeit weakly, due to the fact that sp^2 orbitals are more electronegative than sp^3 orbitals. The 90-mV shift we observe on going from dmb to dpb therefore appears to be quite reasonable when compared to the shift reported by Furue. The change in reduction potential for dpb versus dmb is likewise consistent with an inductive effect when compared to the 540-mV drop reported for the CF_3-bpy analogs relative to bpy. With this analysis we do not rule out the possibility of influence from the π orbitals, but it does appear that the data can be explained satisfactorily without invoking specific π contributions.

Despite the fact that both the oxidative and reductive waves for the complexes are shifted, the data clearly show the individual shifts tend to cancel each other, resulting in a minimal overall change in the apparent ZPE difference between $[Ru(dmb)_3](PF_6)_2$ and $[Ru(dpb)_3](PF_6)_2$. The difference that is revealed from this approximate calculation—on the order of 700 cm^{-1}—indicates that the ground-state/excited-state ZPE separation in $[Ru(dpb)_3](PF_6)_2$ is lower than that of $[Ru(dmb)_3](PF_6)_2$.[55] The electrochemistry therefore supports the conclusion derived from the spectral fitting analysis, namely that the energy gap is not contributing to the observed trend in k_{nr} between these two molecules.

We propose that the reduction in the rate of nonradiative decay is due to extended intraligand delocalization of the π^* electron in the MLCT excited state of $[Ru(dpb)_3](PF_6)_2$. If we assume a one-electron orbital picture in which the extent of charge transfer in the two complexes is approximately the same,

(49) The homogeneous broadening of the individual vibronic transitions characteristic of these complexes in fluid solution at room temperature suggests that low-frequency modes (including the solvent) can be treated classically in the limit $\hbar\omega \ll kT$. This approximation allows for a reduction in the number of fitting parameters and allows each vibronic component to be described by a Gaussian distribution function.

(50) Low-temperature emission spectra in this class of molecules have similar features, implying that there are no dramatic differences in the nature of the vibrational modes that couple to excited-state relaxation.

(51) Maruszewski, K.; Bajdor, K.; Strommen, D. P.; Kincaid, J. R. *J. Phys. Chem.* **1995**, *99*, 6286 and references therein.

(52) It should be noted that this calculation effectively describes the energy separation between the ground state and the Franck−Condon state. Factors such as spin−orbit coupling and outer-sphere reorganization are therefore not accounted for.

(53) The energy of the excited state is gauged by the amount of energy required to both oxidize the metal and reduce the ligand. Thus, it is given by the absolute value of the difference between the $Ru^{II/III}$ and $bpy^{0/-}$ half-wave potentials.

(54) Furue, M.; Maruyama, K.; Oguni, T.; Naiki, M.; Kamachi, M. *Inorg. Chem.* **1992**, *31*, 3792.

(55) While the use of electrochemical data for estimating ZPE differences in these molecules is convenient, it does have its limitations. For example, the fact that spin−orbit coupling is not taken into account makes it difficult to directly ascribe these results to the actual emissive state in question. In addition, neither inner-sphere nor outer-sphere reorganization energies are explicitly accounted for in the electrochemical analysis.

Table 3. Emission Spectral Fitting Parameters for the dpb Series in CH_3CN at 298 K

complex	E_o (cm^{-1})	E_{oo} (cm^{-1})[a]	$\hbar\omega_M$ (cm^{-1})	S_M	$\Delta\bar{\nu}_{0,1/2}$ (cm^{-1})
$[Ru(dmb)_3](PF_6)_2$	15980 ± 60	17310 ± 60	1330	1.05 ± 0.01	1750 ± 30
$[Ru(dmesb)_3](PF_6)_2$	16070 ± 60	17250 ± 60	1330	1.02 ± 0.01	1640 ± 30
$[Ru(dotb)_3](PF_6)_2$	16080 ± 60	17300 ± 60	1330	0.951 ± 0.009	1670 ± 30
$[Ru(dptb)_3]PF_6)_2$	15690 ± 60	16895 ± 60	1320	0.845 ± 0.008	1665 ± 30
$[Ru(dpb)_3](PF_6)_2$	15770 ± 60	17000 ± 60	1330	0.840 ± 0.008	1680 ± 30

[a] E_{oo} calculated from the following equation: $E_{oo} = E_o + (\Delta\bar{\nu}_{0,1/2})^2/(16 \ln 2)k_BT$. The relative uncertainty in the determination of the above parameters was established for all compounds by using data collected in three separate measurements of $[Ru(dpb)_3](PF_6)_2$ in acetonitrile. It is reported above as 2σ where σ is the standard deviation determined in the three analyses of $[Ru(dpb)_3](PF_6)_2$ emission data.

Table 4. Electrochemical Data for the dpb Series in CH_3CN[a]

	3+/2 (V)			1+/2+ (V)			$\Delta E_{(redox)}$	$\Delta E_{(redox)}$	
complex	E_{pc}	E_{pa}	$E_{1/2}$	E_{pc}	E_{pa}	$E_{1/2}$	(V)	(cm^{-1})	D (V)[c]
$[Ru(dmb)_3](PF_6)_2$	1.09	1.18	1.14	−1.465	−1.40	−1.43	2.57	20700	0.42
$[Ru(dmesb)_3](PF_6)_2$	1.20	1.28	1.24	−1.36	1.295	−1.33	2.56	20700	0.42
$[Ru(dotb)_3](PF_6)_2$	1.20	1.27	1.23	−1.32	−1.26	−1.29	2.53	20400	0.38
$[Ru(dptb)_3](PF_6)_2$[b]	1.11	1.22	1.18	−1.32	−1.24	−1.28	2.46	19850	0.37
$[Ru(dpb)_3](PF_6)_2$	1.19	1.26	1.23	−1.28	−1.22	−1.25	2.48	20000	0.37

[a] Scan rate 100 mV s^{-1}; 0.10 M NBu_4PF_6 in CH_3CN. Values given in volts vs SCE. [b] Data are not IR compensated for this case. [c] Calculated with eq 7 and data for E_{oo} from Table 3.

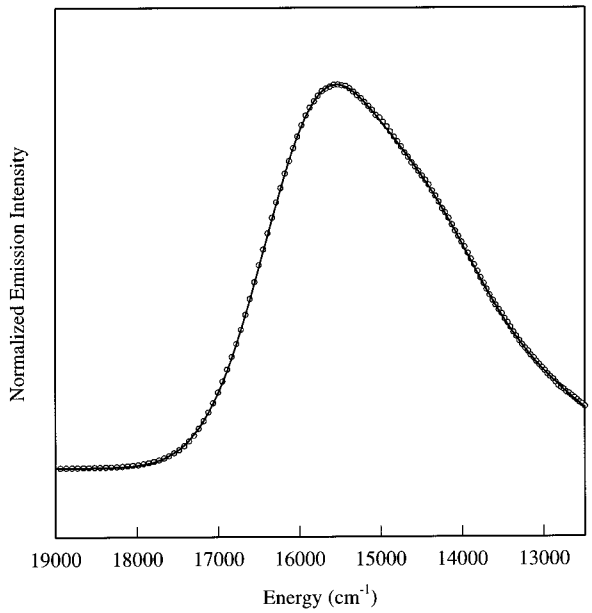

Figure 3. Analysis of the emission spectrum of $[Ru(dpb)_3](PF_6)_2$ in CH_3CN at 298 K according to eq 5. The circles correspond to the experimental spectrum, whereas the solid line indicates the fit. See text for a discussion of the fitting parameters.

allowing the excited electron to delocalize over both the pyridyl and phenyl rings would attenuate the effect of antibonding orbital population by distributing electron density over a larger number of bonds. The net result would be a decrease in ΔQ_e relative to the dmb complex along all coordinates sensitive to electron density in the π^* orbital. The effect would be similar to what is observed in conjugated organic systems, in which one-electron reduction of long-chain conjugated links yields only very small changes in the average C−C bond length relative to shorter chain analogs.[56−61] Similar arguments for rationalizing the photophysical properties of metal-containing systems have been invoked by other workers, most notably Strouse, et al.,[62] who rationalized the unusually long excited-state lifetime of $[(dmb)_2Ru(\mu\text{-bbpe})Ru(dmb)_2]^{4+}$ (where bbpe = *trans*-1,2-bis-(4-(4′-methyl)-2,2′-bipyridyl)ethene) by postulating a small ΔQ_e caused by electron delocalization within the bridging bbpe ligand. In addition, Treadway et al.[8] have recently analyzed a number of MLCT systems from the literature regarding the effects of delocalization and acceptor ligand rigidity on decreasing rates of nonradiative excited-state decay. To achieve delocalization in our system, we postulate that the excited state of $[Ru(dpb)_3](PF_6)_2$ is characterized by a ligand conformation in which the 4,4′-phenyl substituents are coplanar with the bipyridyl fragment. This structural motif is directly analogous to what is observed in biphenyl upon one-electron reduction[63,64] and one that is also implicated in the reduced form of paraquat.[65]

Before leaving this section we wish to point out to the reader that application of the above model (eq 5) to emission spectra results only in a description of vibrational modes that are coupled to *radiative* transitions from the excited state to the ground state. Using information derived from these fits to describe nonradiative processes therefore implicitly assumes that such modes are also coupled to nonradiative decay processes in the molecule. While we agree it is tempting to make such an assumption, we see no reason a priori why radiative and nonradiative decay processes must occur along the same nuclear coordinate(s). The vibrational overlap requirements for radiative and nonradiative decay are quite different insofar as nonradiative surface-to-surface transitions occur along isoenergetic trajectories, whereas radiative transitions are vertical. One could envision a circumstance in which projection of excited- and ground-state potential energy surfaces resulted in a large displacement along one coordinate but not another. Given the right combination of ΔZPE and ΔQ_e, vibrational overlap for nonradiative decay could be favored in the first case, whereas emission might occur via coupling to a totally different coordinate. It does appear to be usually the case that when highly displaced modes are present, nonradiative decay from the excited state dominates and the compounds are nonemissive.

(56) Van Duyne, R. P.; Suchanski, M. R.; Lakovits, J. M.; Siedle, A. R.; Parks, K. D.; Cotton, T. M. *J. Am. Chem. Soc.* **1979**, *101*, 2832.
(57) Takahashi, C.; Maeda, S. *Chem. Phys. Lett.* **1974**, *24*, 584.
(58) Zahradnik, R.; Carsky, P. *J. Phys. Chem.* **1970**, *74*, 1249.
(59) Jeanmarie, D. C.; Van Duyne, R. P. *J. Am. Chem. Soc.* **1976**, *98*, 4029.
(60) Takahashi, C.; Maeda, S. *Chem. Phys. Lett.* **1974**, *28*, 22.
(61) Takahashi, C.; Maeda, S. *Chem. Phys. Lett.* **1973**, *22*, 364.
(62) Strouse, G. F.; Schoonover, J. R.; Duesing, R.; Boyde, S.; Jones, W. E.; Meyer, T. J. *Inorg. Chem.* **1995**, *34*, 473.
(63) de Boer, E.; Klaasen, A. A.; Noordik, J. H. *Pure Appl. Chem.* **1979**, *51*, 73.
(64) Noordik, J. H.; Schreurs, J.; Gould, R. O.; Mooij, J. J.; de Boer, E. *J. Phys. Chem.* **1978**, *82*, 1105.
(65) Schoonover, J. R.; Chen, P. Y.; Bates, W. D.; Dyer, R. B.; Meyer, T. J. *Inorg. Chem.* **1994**, *33*, 793.

In addition, we recognize that in the context of a single configurational coordinate model, such as we have employed here, k_r and k_{nr} must be evaluated along the same coordinate. However, from a theoretical standpoint we do not believe that this is necessarily correct.

The second point concerns the fact that the current model implicitly assumes that the *entire* emission profile is due to radiative coupling to vibrational modes that also give rise to the low-energy structure in the spectrum. There is no direct provision within the model for contributions from radiative transitions along coordinates for which there is no nuclear displacement (e.g., $S_M = 0$). While these coordinates will not significantly affect the asymmetry of the spectral profile, they can contribute strongly to $I(\bar{\nu})$ at or near the origin. This will manifest itself experimentally as a homogeneously broadened Gaussian component superimposed on the emission profile arising from the displaced mode(s). At present we do not believe that neglecting the contribution of nondisplaced modes to $I(\bar{\nu})$ significantly affects trends observed in closely related molecules such as the ones we are examining here, but we are unsure as to its impact on the absolute numbers obtained from the analysis on a given molecule.

Radiative Decay Rates. An examination of Table 2 reveals that, in addition to a drop in k_{nr}, there is also a substantial increase in the overall rate constant(s) for radiative ^{3}MLCT $\rightarrow$ $^1A_1$ decay upon going from $[Ru(dmb)_3](PF_6)_2$ to $[Ru(dpb)_3](PF_6)_2$. On the basis of Fermi's Golden Rule,[66,67] the rate of radiative decay is proportional to the product of the square of the transition dipole moment and the cube of the energy separation between two radiatively coupled states, eq 6:

$$k_r \propto \langle \vec{\mu} \rangle^2 (\bar{\nu})^3 \qquad (6)$$

Thus, both the size of the radiative energy gap between the ^{3}MLCT and $^1A_1$ states (i.e., the energy of emission) and the magnitude of the transition dipole influence k_r. If we consider only $\bar{\nu}$, the predicted trend from eq 6 for these two compounds is opposite from what is experimentally observed: according to eq 6, k_r should be smaller in $[Ru(dpb)_3](PF_6)_2$ due to its slightly lower emission energy.

Since a change in $\bar{\nu}$ cannot account for the differences in k_r, eq 6 indicates that, in the limit of roughly constant electronic coupling,[68] the transition dipole moment for the excited state $\rightarrow$ ground state transition must be larger in $[Ru(dpb)_3](PF_6)_2$. Again, we believe our model of intraligand excited-state delocalization in $[Ru(dpb)_3](PF_6)_2$ adequately accounts for the relative values of k_r between these two molecules. The excited-state transition dipole is a vectorial quantity proportional to the magnitude of the charges times distance separating them. Assuming that the extent of charge transfer is approximately the same in these two compounds, eq 6 and the observed values of k_r imply that the average distance between the electron in the ligand orbital and the metal center is greater in $[Ru(dpb)_3](PF_6)_2$ than in $[Ru(dmb)_3](PF_6)_2$. Delocalization into the peripheral 4,4′-phenyl rings should increase this distance r, thereby increasing the magnitude of the transition dipole and subsequently the cross-section for radiative decay.

Table 5. Results from ab Initio Calculations of Singly-Reduced 4-Phenylpyridine

method/basis set	energy (hartrees) $\theta = 0°$ (NIMAG)[a]	ΔE_θ $\theta = 44.6°$ [c]
UHF/3-21+G(d)	−473.610077 (0)	6.53 kcal/mol
UHF/6-31+G(d)	−476.236776 (0)	7.34 kcal/mol
MP2/6-31+G(d)[b]	−477.779204	6.32 kcal/mol

[a] NIMAG = number of imaginary frequencies. [b] MP2/6-31+G(d) calculations were done as a single point. [c] Value of θ was chosen from MP2/6-31+G(d) calculation of neutral 4-phenylpyridine.

Ab Initio Calculations. In addition to spectroscopic evidence, we have used ab initio calculations to explore whether the ligand electronic structure of the MLCT excited state of $[Ru(dpb)_3](PF_6)_2$ is best described as delocalized between the bipyridine and its substituent phenyl rings. There is considerable literature precedent for the theoretical study of biphenyl in its neutral, cationic, and anionic forms,[69−72] systems to which a clear analogy can be drawn to the aryl-pyridine fragments present in dpb. In our computational model, we have made two significant approximations. The first is that, although the metal is a substantial perturbation to the overall electronic structure of the ligand, we suggest that metal−ligand interactions in the ground state are not significantly different from those in the excited state. We have, therefore, studied an isolated model ligand rather than the full $[Ru(dpb)_3]^{2+}$ metal complex. The second approximation concerns the size of the ligand itself. Rather than computationally treating the phenyl-substituted bipyridines, we have used 4-phenylpyridine as a model for the ground-state ligand geometry and (4-phenylpyridine)$^-$ to describe the MLCT ligand excited-state geometry. We believe that in these smaller systems, the aryl-pyridine π interactions should be indicative of those taking place in dpb and dpb$^-$. These approximations afford us a more computationally feasible problem, one in which we can use extensive basis sets to create the relevant ligand molecular orbitals.

Results of calculations on the neutral 4-phenylpyridine will be discussed later in this paper. It is worth noting here, however, that in this model of the ground-state ligand geometry the lowest energy conformation is one in which there is a 45° twist angle between the phenyl and pyridine ring systems (MP2/6-31G(d)). While the π-systems of these two rings are not completely orthogonal, it reasonable to assume that π-interactions between them are attenuated. On the other hand, in our computational model of the excited-state ligand geometry (i.e., (4-phenylpyridine)$^-$), the lowest energy conformation is one in which the two ring systems are coplanar. Unrestricted Hartree−Fock (UHF) methods and second-order perturbation theory show that this is the case for each of the three methods/basis sets employed (Table 5). Frequency calculations with UHF methods suggest that there are zero imaginary frequencies, indicating that the coplanar geometry is a stationary-state minimum. Due to the diffuse functions used in the basis sets for the anion, it was computationally unfeasible to do full geometry optimization and frequency analysis at the MP2/6-31+G(d) level. As such, the coplanar MP2 calculation was done as a single point calcu-

(66) Levich, V. G. *Physical Chemistry: An Advanced Treatise*; Eyring, H., Henderson, D., Eds.; Academic Press: New York, 1970; Vol. 9B.

(67) Kestner, N. R.; Logan, J.; Jortner, J. *J. Phys. Chem.* **1974**, *78*, 2148.

(68) Watts and Crosby (cf. ref 35) invoke changes in electronic coupling to account for their observations on $[Ru(dpb)_3](PF_6)_2$ at 77 K. We do not necessarily dispute their interpretation for two reasons. First, we believe that a comparison of data between glass and fluid solution is problematic, particularly in the present system where we believe significant molecular motion accompanies excited-state relaxation. Second, given the strongly vibronic nature of this system as evidenced by our data, making a distinction between electronic and geometric factors may not be reasonable. We simply point out that all of our results can be explained quite well in the context of a model in which vibrational factors change significantly, but electronic factors do not.

(69) Rubio, M.; Merchan, M.; Orti, E. *Theor. Chim. Acta* **1995**, *91*, 17.

(70) Rubio, M.; Merchan, M.; Orti, E.; Roos, B. O. *J. Phys. Chem.* **1995**, *99*, 14980.

(71) Rubio, M.; Merchan, M.; Orti, E.; Roos, B. O. *Chem. Phys. Lett.* **1995**, *234*, 373.

(72) Tsuzuki, S.; Tanabe, K. *J. Phys. Chem.* **1991**, *95*, 139.

Table 6. Selected Bond Distances and Angles for $[Ru(dmesb)_3](PF_6)_2$

	Distances (Å)		
Ru(1)−N(1)	2.051(5)	C(3)−C(6)	1.507(9)
Ru(1)−N(2)	2.053(5)	C(17)−C(20)	1.492(9)
Ru(1)−N(3)	2.104(5)	C(31)−C(34)	1.492(9)
Ru(1)−N(4)	2.111(6)	C(45)−C(48)	1.486(9)
Ru(1)−N(5)	2.064(5)	C(59)−C(62)	1.482(9)
Ru(1)−N(6)	2.068(5)	C(73)−C(76)	1.482(9)
	Angles (deg)		
N(1)−Ru(1)−N(2)	78.4(2)	N(2)−Ru(1)−N(6)	93.5(2)
N(1)−Ru(1)−N(3)	97.9(2)	N(3)−Ru(1)−N(4)	77.5(2)
N(1)−Ru(1)−N(4)	91.1(2)	N(3)−Ru(1)−N(5)	90.3(2)
N(1)−Ru(1)−N(5)	169.1(2)	N(3)−Ru(1)−N(6)	94.0(2)
N(1)−Ru(1)−N(6)	94.0(2)	N(4)−Ru(1)−N(5)	97.8(2)
N(2)−Ru(1)−N(3)	171.8(2)	N(4)−Ru(1)−N(6)	170.6(2)
N(2)−Ru(1)−N(4)	95.2(2)	N(5)−Ru(1)−N(6)	78.2(2)
N(2)−Ru(1)-N(5)	94.4(2)		

lation based on the full geometry optimization done at UHF/6-31+G(d). Also indicated in Table 5 is a column for ΔE_θ: values which represent the energetic cost on going from a coplanar geometry to one in which the twist angle between the ring systems is forced to stay at 45° (vide infra). It is evident that there is a considerable thermodynamic driving force—on the order of 7 kcal/mol—for achieving a coplanar delocalized structure in the reduced species. To illustrate the origin of this stabilization, we can invoke a useful resonance picture often used in the context of reduced biphenyl in which there is double-bond character between the two ring systems:

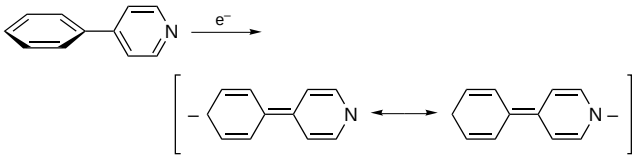

In fact, a molecular orbital picture generated for the SOMO of (4-phenylpyridine)$^-$ (UHF/6-31+G(d)) indicates strong π-bonding between the two rings. More details concerning these calculations will be discussed at length elsewhere.[73]

II. Synthetic Control: Steric Tuning of Excited-State Delocalization. If the unusual photophysical properties of $[Ru(dpb)_3](PF_6)_2$ are indeed caused by coplanarity of the bipyridyl and phenyl fragments in the excited state, then it should be possible to modulate the extent of intraligand delocalization by altering the degree to which the phenyl substituent can rotate into the plane of the bpy ligand. For example, if bulky functional groups are placed at positions adjacent to the 4,4′ positions of the bipyridine (either on the pyridine rings or the phenyl rings), a steric barrier to forming a planar species would be introduced. In addition to substantiating our physical model for excited-state delocalization in $[Ru(dpb)_3](PF_6)_2$, such a study would also demonstrate that one can manipulate the photophysical properties of molecules by controlling the extent of delocalization in the excited state through synthetic means. The strategy is similar in principal to that used by many workers in this field with regard to excited-state energies (i.e., ΔZPE). In the present case, tunability of photophysical behavior would be achieved through variations in ΔQ_e as opposed to E_{00} and would establish a second mechanism by which excited-state properties can be tailored.

We have synthesized a series of molecules in which steric bulk is used to modulate the degree of extended, ligand-based delocalization. The ligands, comprising what we refer to as the "dpb series", are illustrated below.

(73) Damrauer, N. H.; McCusker, J. K. Manuscript in preparation.

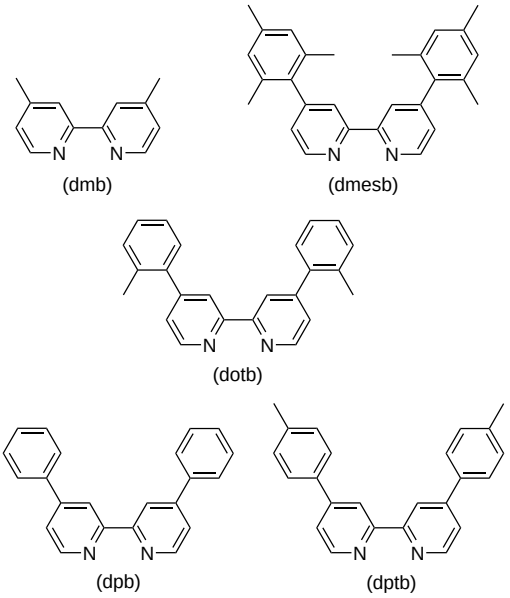

The new ligands—dotb, dmesb, and dptb—were all synthesized by the same general method via Suzuki coupling of 4,4′-dibromo-2,2′-bipyridine with the appropriate boronic acid.

A single-crystal X-ray structure determination was carried out on $[Ru(dmesb)_3](PF_6)_2$. Crystallographic data are given in Table 1, and selected bond distances and angles are given in Table 6. A computer drawing of the cation is shown in Figure 4. The core structure of the cation is very similar to that found for $[Ru(bpy)_3]^{2+}$ and other crystallographically characterized members of this class, with Ru^{II}−N bond lengths on the order of 2.06 Å. Bond angles both around the metal center and within the pyridyl and phenyl rings are also unremarkable. The most important aspect of this structure for the purposes of this study are the dihedral angles between the planes defined by the individual pyridyl rings and the peripheral mesityl groups, respectively. Averaging over the six dihedral angles of the complex affords a value of $\sim 70 \pm 10°$. This severe canting of the mesityl substituent with respect to the bound pyridine is no doubt a result of steric interactions between the methyl groups ortho to the C−C link and the 3 and 5 protons of the pyridine. It is interesting to note that, although strongly canted, the most sterically favored geometry of $\theta = 90°$ is not achieved. It is difficult to attribute this to any one factor, but it may reflect a balance between steric interactions and an energetic stabilization of a planar configuration (vide infra). In addition, it should be noted that the orientation of the mesityl substituents varies, with two of the bipyridines having their mesityl groups canted toward each other, while in the third, the mesityl groups are canted in the same direction. Again, with the caveat that packing forces might be playing a role (although no close contacts are seen in the packing diagram), the fairly wide range in θ is suggestive of a very soft potential and a relatively low barrier through the 90° configuration. Overall, the main factor to be gleaned from this structure is that the steric bulk introduced on the peripheral phenyl ring is severely hindering co-planarity of the bipyridine with the phenyl substituents, correspondingly attenuating any extended π interactions among the four ring systems.

The dotb and dmesb ligands represent stepwise increases in steric hindrance to a planar delocalized structure. According to our model, we anticipate that as the degree of steric bulk on the peripheral phenyl ring increases (i.e., dpb ⇒ dotb ⇒ dmesb), we should observe a decrease in k_r, an increase in k_{nr}, and corresponding changes in the Huang−Rhys factor S_M such that

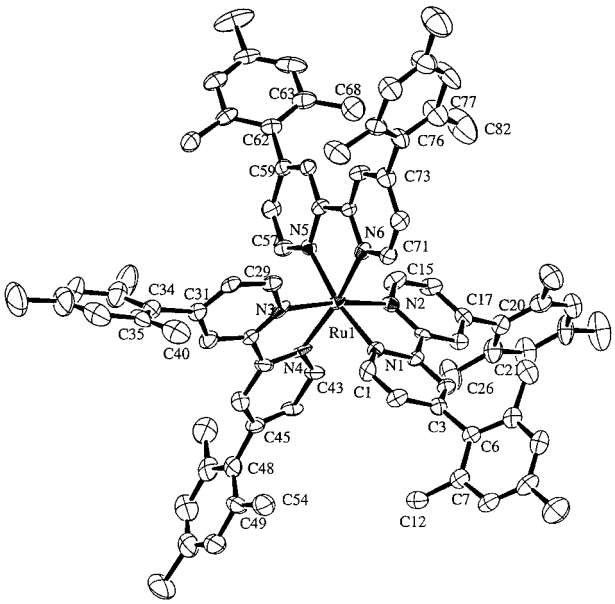

Figure 4. Drawing of the cation of $[Ru(dmesb)_3](PF_6)_2$ from a single-crystal X-ray structure determination. See Table 1 for crystallographic details and Table 6 for structural details.

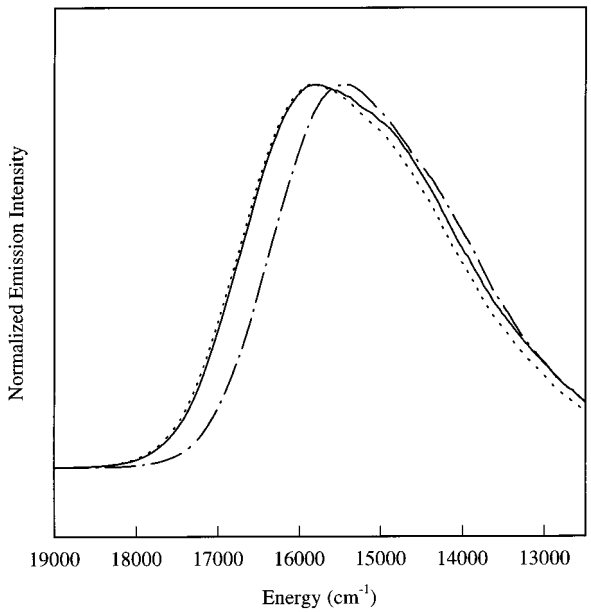

Figure 5. Emission spectra of $[Ru(dmesb)_3](PF_6)_2$ (solid line), $[Ru(dotb)_3](PF_6)_2$ (dotted line), and $[Ru(dptb)_3](PF_6)_2$ (dashed line), all in deoxygenated CH_3CN solution at 298 K.

$S_M(dpb) < S_M(dotb) < S_M(dmesb)$. In the limit that the two ortho methyl groups in dmesb totally inhibit the formation of a planar species, we would expect the photophysical properties of $[Ru(dmesb)_3](PF_6)_2$ to be reminiscent of $[Ru(dmb)_3](PF_6)_2$, with $[Ru(dotb)_3](PF_6)_2$ lying somewhere between the two parent compounds $[Ru(dmb)_3](PF_6)_2$ and $[Ru(dpb)_3](PF_6)_2$. The dptb ligand, like dpb, has no additional steric hindrance to planarity and was made, rather, to monitor that changes in photophysical properties were not attributable to either differences in solvation among the various compounds or inductive effects due to methylation of the phenyl substitutent.

Excited-State Properties of the dpb Series: Emission. The same photophysical probes used to characterize $[Ru(dmb)_3](PF_6)_2$ and $[Ru(dpb)_3](PF_6)_2$ were also employed for the three methylated analogs. Emission spectra collected for $[Ru(dptb)_3](PF_6)_2$, $[Ru(dotb)_3](PF_6)_2$, and $[Ru(dmesb)_3](PF_6)_2$ in CH_3CN are illustrated in Figure 5; data on emission quantum yields and rate constants for radiative and nonradiative decay are summarized in Table 2. The data collected on $[Ru(dpb)_3](PF_6)_2$ and $[Ru(dptb)_3](PF_6)_2$ are very similar, indicating that methylation of the phenyl rings in a sterically nondemanding position does not significantly alter the excited-state properties of the compound. Data across the methylated series, where the steric hindrance to planarity is increasing, show a clear trend in photophysical parameters: an increase in k_{nr} and a decrease in k_r. By $[Ru(dmesb)_3](PF_6)_2$ in the series, k_{nr} is comparable to, if slightly smaller than, $[Ru(dmb)_3](PF_6)_2$.

Spectral fitting parameters for all of the complexes in CH_3CN are given in Table 3. The first point to note is that there does not appear to be any significant trend in either E_0 or E_{00} across the series. This is illustrated further in the electrochemical data (Table 4), in which we see fairly minimal variations in the calculated values of ΔZPE. What is significant, however, is the trend in S_M. We see a clear progression in the Huang−Rhys factor from a value for $[Ru(dptb)_3](PF_6)_2$ essentially identical with that of $[Ru(dpb)_3](PF_6)_2$ (0.845 versus 0.840) to a value for $[Ru(dmesb)_3](PF_6)_2$ similar to, although slightly smaller than, that determined for $[Ru(dmb)_3](PF_6)_2$. Lying approximately halfway in between is $[Ru(dotb)_3](PF_6)_2$, consistent with its "intermediate" degree of steric bulk as compared to the *p*-tolyl and mesityl species. The spectral fitting therefore supports the notion that, as the amount of steric hindrance toward forming a planar ligand species is increased, the degree of excited-state distortion as gauged by ΔQ_e also increases.

Electrochemical *D* Parameter. In addition to static and time-resolved emission data, the effects of intraligand delocalization are also evident from the electrochemical data within the context of a formalism recently introduced by Vlcek and co-workers.[74] It was mentioned earlier that gleaning information about ZPE differences from electrochemical data in these types of systems involves some approximations and the unavoidable neglect of certain terms.[52,55] Although the observed trends are consistent with the more detailed spectral fitting analysis, the exact values obtained by the two methods are significantly different. Vlcek et al. have proposed a model that compensates for the discrepancy inherent in such an analysis. On the basis of a wide sampling of Ru diimine complexes (∼70), these authors have suggested the following relationship:

$$\Delta E_{(redox)} = E_{00} + D \qquad (7)$$

where D is related, in a one-electron approximation, to the Coulomb repulsion energy $J_{a,x}$ of an electron in a ligand orbital (x) and an electron in a metal dπ valance orbital (a), plus the appropriate solvation energy difference. Qualitatively, this means that the larger the value of D, the greater the electron−electron repulsion between the ligand-centered and metal-centered electrons of the reduced complex. Using eq 7, electrochemical data (Table 4), and spectral fitting parameters (Table 3), we have calculated our own values of D for the dpb series (Table 4). Making the assumption that the energetics of solvation are roughly the same for the aryl-substituted molecules, we see that the value of D for $[Ru(dmesb)_3](PF_6)_2$ is significantly larger than that calculated for $[Ru(dpb)_3](PF_6)_2$ and $[Ru(dptb)_3](PF_6)_2$. In other words, an estimate of E_{00} from $\Delta E_{(redox)}$ requires a larger energetic correction for $[Ru(dmesb)_3](PF_6)_2$ than is necessary for $[Ru(dpb)_3](PF_6)_2$ or $[Ru(dptb)_3](PF_6)_2$. We suggest that this difference in D is indicative of the degree of delocalization that these molecules achieve in their singly reduced forms. On average, more extended delocalization of

(74) Vlcek, A. A.; Dodsworth, E. S.; Pietro, W. J.; Lever, A. B. P. *Inorg. Chem.* **1995**, *34*.

the electron in the ligand orbital would allow it to occupy space further away from the metal center. This should translate into an overall decrease in electron−electron repulsion between the ligand- and metal-centered electrons, thereby reducing the magnitude of $J_{a,x}$. Our interpretation of the relative rates of radiative decay in these complexes is also consistent with this kind of an increase in the magnitude of the metal−ligand electric dipole vector for the $[Ru(dpb)_3](PF_6)_2$ and $[Ru(dptb)_3](PF_6)_2$ excited states (vide supra).

Time-Resolved Resonance Raman. The notion that the degree of excited-state distortion is coupled to differences in the extent of intraligand electron delocalization can be examined further by using time-resolved resonance Raman spectroscopy. In the one-color experiment, the 355 nm excitation pulse both creates the excited state and acts as a source for Raman scatter off the excited state. Resonance Raman spectra of the ^{3}MLCT excited states were obtained on CH_3CN solutions of each molecule. For purposes of comparison, we will focus the discussion on $[Ru(dpb)_3]^{2+}$ and $[Ru(dmesb)_3]^{2+}$. The ground-state and excited-state resonance Raman spectra of $[Ru(dmesb)_3]^{2+}$ are shown in the top part of Figure 6. The ground-state spectrum consists of a series of resonantly enhanced vibrational modes associated with direct excitation into the metal-to-ligand charge transfer band. The spectrum of $[Ru(bpy)_3]^{2+}$ has been extensively studied and the spectral assignments supported by normal coordinate analysis.[75,76] In the case of $[Ru(dmesb)_3]^{2+}$, we can, by inference to the $[Ru(bpy)_3]^{2+}$ spectrum, associate the band at 1615 cm^{-1} to ring stretches of the pyridyl and/or phenyl rings. Other bands observed in the spectrum are reminiscent of what is observed in both $[Ru(bpy)_3]^{2+}$ and $[Ru(dmb)_3]^{2+}$, but are more difficult to assign by comparison due to the increased vibrational complexity of the $[Ru(dmesb)_3]^{2+}$ system.

Two sets of bands are clearly evident in the transient spectrum. One set of bands is identical in frequency with bands measured in the ground-state spectrum while the other vibrational modes are shifted from the ground-state vibrations. If we adopt the excited-state formalism as $[Ru^{III}(dmesb)_2(dmesb^-)]^{2+}$,[77] the latter modes are associated with the localization of the excited-state electron on one of the dmesb ligands, while the former arise from neutral ligands (NL) also present in the excited state. Both sets of vibrations are usually observed due to the overlap at the excitation frequency of the $\pi \rightarrow \pi^*$ of the neutral bipyridine ligands and the absorption of the radical anion. At the power levels investigated (3−5 mJ/pulse), we see no evidence for resonance Raman scatter from ground-state molecules. However, at lower power levels (<3 mJ/pulse), the ratio of the intensity from NL modes to excited-state bands does increase, suggesting contribution from ground-state molecules. The spectra are complex, and a complete assignment is not possible in the absence of a normal coordinate analysis. However, referring back to the 1615-cm^{-1} mode identified in the ground-state spectrum, we can assign a band in the excited-state spectrum at 1548 cm^{-1} as the corresponding ring-stretching mode of the reduced ligand. The decrease in vibrational frequency of this ring stretch is similar to what is observed in the excited-state resonance Raman spectra of both $[Ru(bpy)_3]^{2+}$ and $[Ru(dmb)_3]^{2+}$ and is consistent with the photophysical data described above, indicating that the degree of excited-state distortion in $[Ru(dmesb)_3]^{2+}$ is very similar to that of $[Ru(dmb)_3]^{2+}$.

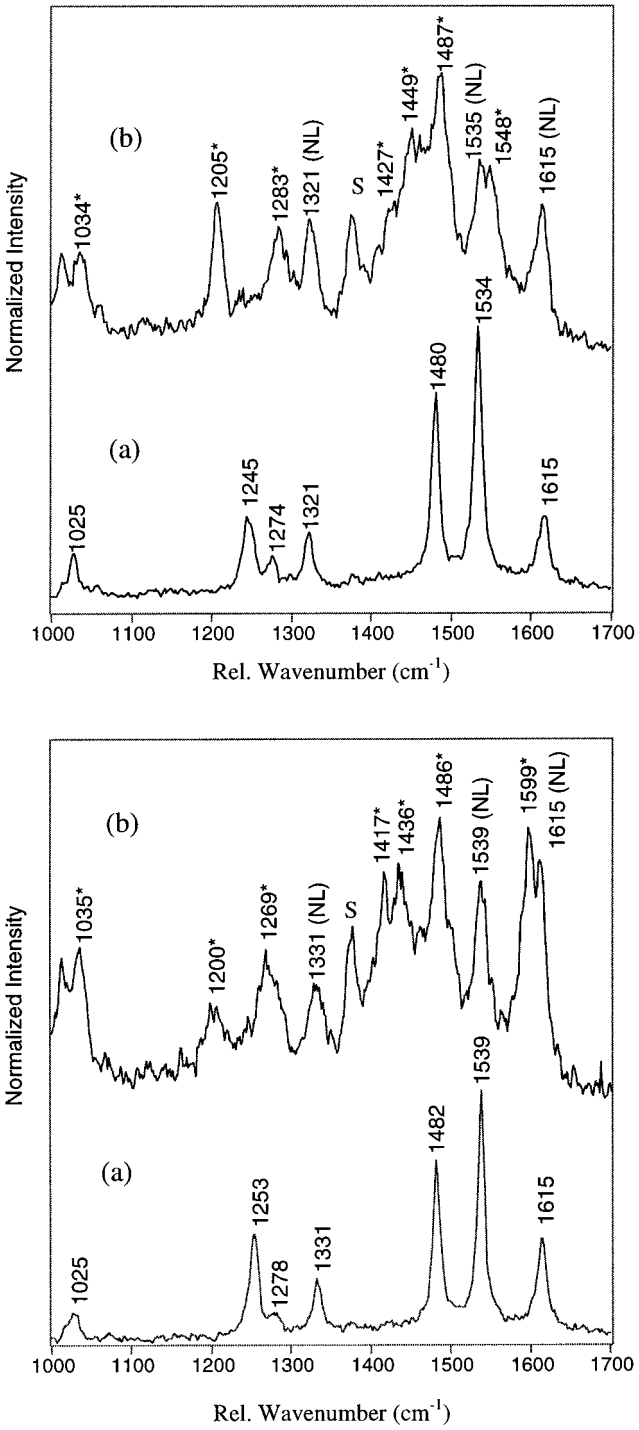

Figure 6. Top: Ground-state (a) and excited-state (b) resonance Raman spectra for $[Ru(dmesb)_3](PF_6)_2$ in degassed CH_3CN solution. The peaks marked with an asterisk in the excited-state spectrum are assigned to vibrations of the reduced ligand (i.e., $dmesb^-$ of the $[Ru(dmesb)_2(dmesb^-)]^{2+}$ excited state), whereas neutral ligand vibrations are designated as NL. The peak at ca. 1400 cm^{-1} in the excited-state spectrum is due to solvent (S). Bottom: Ground-state (a) and excited-state (b) resonance Raman spectra for $[Ru(dpb)_3](PF_6)_2$ in degassed CH_3CN solution. The peaks marked with an asterisk in the excited-state spectrum are assigned to vibrations of the reduced ligand (i.e., dpb^- of the $[Ru(dpb)_2(dpb^-)]^{2+}$ excited state), whereas neutral ligand vibrations are designated as NL. The peak at ca. 1400 cm^{-1} in the excited-state spectrum is due to solvent (S). See text for further details.

The ground- and excited-state resonance Raman spectra of $[Ru(dpb)_3]^{2+}$ are shown in the bottom portion of Figure 6.[78] It can be seen that the ground-state spectrum for $[Ru(dpb)_3]^{2+}$ is

(75) Mallick, P. K.; Danzer, G. D.; Strommen, D. P.; Kincaid, J. R. *J. Phys. Chem.* **1988**, *92*, 5628.

(76) Strommen, D. P.; Mallick, P. K.; Danzer, G. D.; Lumpkin, R. S.; Kincaid, J. R. *J. Phys. Chem.* **1990**, *94*, 1357.

(77) We adopt a localized picture of the excited state of these molecules under our experimental conditions, i.e., fluid solution.

nearly identical with that of $[Ru(dmesb)_3]^{2+}$. However, differences are observed in the excited-state spectrum. Most significantly, we observe a much smaller shift of the 1615-cm^{-1} band to only 1599 cm^{-1} in $[Ru(dpb)_3]^{2+}$, 51 cm^{-1} higher in energy than the corresponding band in $[Ru(dmesb)_3]^{2+}$. Reduction of the ligand in the excited state results in a much smaller perturbation of the ring-stretching frequency in $[Ru(dpb)_3]^{2+}$. We interpret this as strong support of our model for extended intraligand electron delocalization and the notion that the geometric distortion of the excited state is much smaller in $[Ru(dpb)_3]^{2+}$ than in the more sterically demanding $[Ru(dmesb)_3]^{2+}$. Increasing the number of bonds over which the electron in the excited state can delocalize attenuates the degree of antibonding character per C−C or C−N bond, thereby leading to a smaller change in the measured vibrational frequency commensurate with the smaller change in effective bond order.

Ground- and excited-state resonance Raman spectra were also collected on a CH_3CN solution of $[Ru(dotb)_3]^{2+}$. The time-resolved spectrum for this compound is dominated by ground-state bands, suggesting that the excited state of this complex is a poorer scatterer than either $[Ru(dpb)_3]^{2+}$ or $[Ru(dmesb)_3]^{2+}$. In addition, the reduced symmetry of the complex relative to other members of the series makes a direct comparison difficult due to the presence of several more bands in both the ground-state and excited-state spectra. We can ascribe a shift from 1618 cm^{-1} in the ground state to 1576 cm^{-1} in the excited state as corresponding to the ring vibration discussed above. This excited-state band falls between the dpb and dmesb complexes, consistent with the ligand's "intermediate" degree of steric bulk. However, this assignment must be considered tentative until a more detailed analysis of this system, possibly with the use of isotopic substitution, can be undertaken.

Excited-State Absorption. We have collected nanosecond time-resolved difference absorption spectra for the full series of molecules discussed herein. The trend in transient absorption features across the dpb series not only illustrates the basic excited-state absorption features of these molecules, but also provides compelling evidence for our model on the effect of sterics and the ability of the ligand to adopt a planar configuration in the excited state.

Spectroelectrochemical measurements have proven to be useful in helping to identify absorptive features associated with MLCT excited states.[79,80] In Figure 7 are shown a portion of the spectrum of dpb^-, prepared by addition of a slight stoichiometric excess of Na to a THF solution of the neutral ligand, along with the excited-state/ground-state difference absorption spectrum of $[Ru(dpb)_3](PF_6)_2$ in CH_3CN following nanosecond excitation at 460 nm. A visual comparison between the dpb^- spectrum and the transient difference spectrum strongly suggests that the ^{3}MLCT excited-state absorption in $[Ru(dpb)_3](PF_6)_2$ at 540 nm is a ligand-based transition, presumably $\pi \rightarrow \pi^*$ or $\pi^* \rightarrow \pi^*$ in nature. The red shift from 500 nm observed for the reduced free ligand is likely due to either stabilization of the π^* and/or destabilization of the π orbitals resulting from interaction with the metal center or is an apparent red shift due to the concomitant bleach of ground-state absorption features (vide infra). It should be pointed out that the ground state has relatively little absorptive cross-section for $\lambda > 525$ nm so the difference spectrum in this region should bear a strong resemblance to the true excited-state absorption spectrum (vide infra).

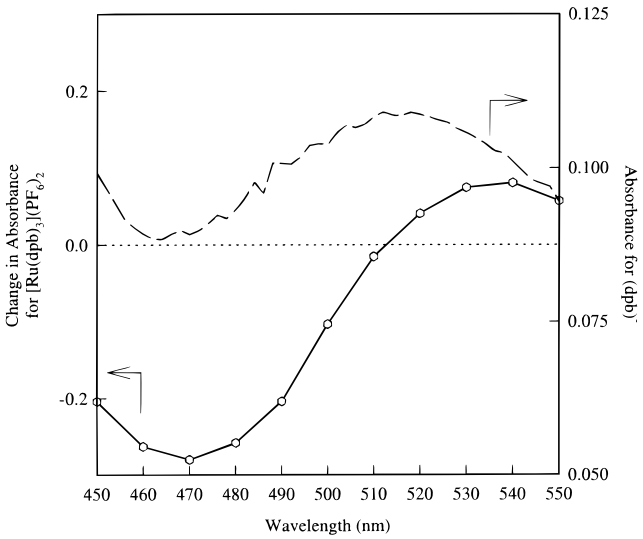

Figure 7. Overlay of the absorption spectrum of dpb^- (dashed line, right-hand *y*-axis) with the excited-state absorption difference spectrum of $[Ru(dpb)_3](PF_6)_2$ in deoxygenated CH_3CN solution following nanosecond excitation at 460 nm (solid line with symbols, left-hand *y*-axis). The bleach centered at 470 nm in the difference spectrum is largely due to loss of ground-state absorption, while the positive feature at $\lambda > 510$ nm is assigned as a predominantly ligand-based absorption of the dpb radical anion present in the ^{3}MLCT excited state.

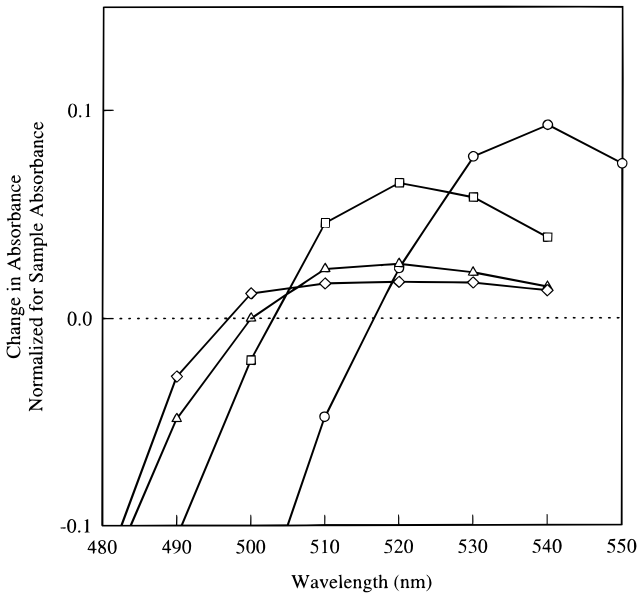

Figure 8. Overlay of the excited-state absorption difference spectra of $[Ru(dmb)_3](PF_6)_2$ (diamonds), $[Ru(dmesb)_3](PF_6)_2$ (triangles), $[Ru(dotb)_3](PF_6)_2$ (squares), and $[Ru(dptb)_3](PF_6)_2$ (circles) in deoxygenated CH_3CN solution following nanosecond excitation at 460 nm. Only the region of the low-energy ligand-based absorption is shown. The increase in intensity is attributed to an increased degree of intraligand electron delocalization across the series.

Nanosecond time-resolved excited-state absorption difference spectra for all compounds in the dpb series collected in CH_3CN solution at room temperature are illustrated in Figure 8. For these experiments, care was taken to ensure that the laser intensity and pump-probe cross-section were kept approximately constant across the series. In addition, the spectra have been normalized for sample absorbance at the excitation wavelength (460 nm). Assuming that the quantum yield for forming the

(78) Kumar, C. V.; Barton, J. K.; Gould, I. R.; Turro, N. J.; Van Houten, J. *Inorg. Chem.* **1988**, *27*, 648. These authors have reported the resonance Raman spectra of $[Ru(dpb)_3]^{2+}$ at lower resolution.

(79) Creutz, C.; Chou, M.; Netzel, T. L.; Okumura, M.; Sutin, N. *J. Am. Chem. Soc.* **1980**, *102*, 1309.

(80) Braterman, P. S.; Song, J.-I.; Peacock, R. D. *Inorg. Chem.* **1992**, *31*, 555.

^{3}MLCT state is the same for all of the molecules in the series, we believe that it is valid to directly compare the difference spectra. It can be seen that there is a clear progression in the spectra with regard to the intensity of the low-energy feature. Specifically, as the steric requirement of the ligand is relaxed (i.e., dmesb ⟹ dotb ⟹ dptb/dpb), we observe an increase in the intensity of this excited-state absorption. We interpret the trend as being consistent with favoring ligand planarity in the ^{3}MLCT state(s) of these phenyl-substituted systems whereby the magnitude of the excited-state absorption cross-section is dependent on the degree of delocalization in the largely ligand-based excited state. The apparent red shift is intriguing but must be treated with some caution. Similar red shifts have been observed for the extended π systems of organic aromatics such as polyacetylene.[81] It is well-known that as the degree of conjugation increases in such systems, the π^* orbitals in particular become stabilized, which results in a red shift of the lowest-energy absorption band. In the same way, it appears that the ca. 20-nm shift in excited-state absorption maxima from $[Ru(dmb)_3](PF_6)_2$ to $[Ru(dptb)_3](PF_6)_2$ suggests increased conjugation (i.e., delocalization) in $[Ru(dptb)_3](PF_6)_2$. As expected, the other two compounds exhibit excited-state absorption maxima that fall in between these two extremes. However, these are not absolute excited-state absorption spectra but rather excited-state difference spectra. The ground-state ^{1}MLCT absorption also red shifts within this series with decreasing steric bulk (vide infra). Therefore, the ground-state bleach upon formation of the ^{3}MLCT excited state may be responsible for the apparent red shifting of excited-state absorptions within this series of molecules. It is clear that absolute excited-state absorption features need to be measured to definitively comment on the nature of the apparent red shift. We are currently working toward this according to methods described by Hoffman et al.[82] as well as our own experimental design for measuring quantum yields of excited-state formation.

Ground-State Structure. The crystal structure of $[Ru(dmesb)_3](PF_6)_2$ was described above. It is clear from Figure 4 that the mesityl ring is canted with respect to the pyridyl rings in the ground state. As discussed above, this canting is apparently retained to a large extent in the excited state, and its ground- and excited-state structures are consistent with our expectations of the steric influence of the ortho methyl groups of the mesityl. We have been unable to grow X-ray quality single crystals of either $[Ru(dpb)_3](PF_6)_2$ or $[Ru(dptb)_3](PF_6)_2$, so we do not know the specific orientation of the 4,4′-phenyl rings in these compounds. However, we were able to isolate crystals of another compound, $[Ru(dmb)_2(dpb)](PF_6)_2$. This complex is being studied in the context of another project in our laboratory, but its structural features will be of use here to give an indication of the geometry of the dpb ligand in the ground state. A drawing of the cation is shown in Figure 9 with crystallographic data given in Table 1 and skeletal bond distances and angles given in Table 7. The Ru atom is octahedrally coordinated by the nitrogen atoms of the ligands. The Ru−N distances show no particular pattern, and are all within 3σ of the average value of 2.057 Å. Distances and angles within the ligands also appear to be in the normal range and are similar to the $[Ru(dmesb)_3](PF_6)_2$ structure described above. For our purposes, the most important aspect of the structure is the dihedral angle between the two phenyl rings and their associated pyridyl rings of the dpb ligand. The crystal structure

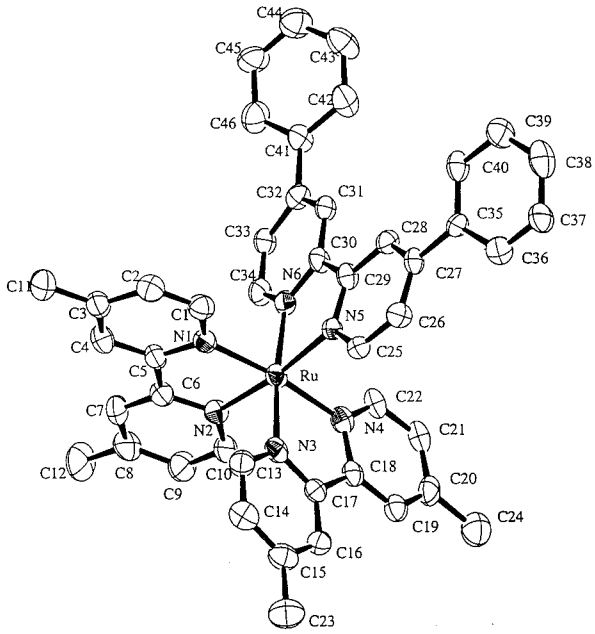

Figure 9. Drawing of the cation of $[Ru(dmb)_2(dpb)](PF_6)_2 \cdot C_7H_8$ from a single-crystal X-ray structure determination. See Table 1 for crystallographic details and Table 7 for structural details.

Table 7. Selected Bond Distances and Angles for $[Ru(dmb)_2(dpb)](PF_6)_2 \cdot C_7H_8$

Distances (Å)			
Ru(1)−N(1)	2.058(6)	C(3)−C(11)	1.50(1)
Ru(1)−N(2)	2.055(5)	C(8)−C(12)	1.50(1)
Ru(1)−N(3)	2.069(6)	C(15)−C(23)	1.49(1)
Ru(1)−N(4)	2.053(6)	C(20)−C(24)	1.50(1)
Ru(1)−N(5)	2.048(5)	C(27)−C(35)	1.483(9)
Ru(1)−N(6)	2.061(6)	C(32)−C(41)	1.501(10)
Angles (deg)			
N(1)−Ru(1)−N(2)	78.6(2)	N(2)−Ru(1)−N(6)	94.6(2)
N(1)−Ru(1)−N(3)	95.8(2)	N(3)−Ru(1)−N(4)	79.3(2)
N(1)−Ru(1)−N(4)	172.9(2)	N(3)−Ru(1)−N(5)	97.7(2)
N(1)−Ru(1)−N(5)	97.5(2)	N(3)−Ru(1)−N(6)	96.0(2)
N(1)−Ru(1)−N(6)	89.2(2)	N(4)−Ru(1)−N(5)	88.3(2)
N(2)−Ru(1)−N(3)	89.6(2)	N(4)−Ru(1)−N(6)	96.0(2)
N(2)−Ru(1)−N(4)	96.2(2)	N(5)−Ru(1)−N(6)	78.3(2)
N(2)−Ru(1)−N(5)	172.0(2)		

reveals this angle to be $28 \pm 1°$ (average). The ground state of the dpb ligand is therefore significantly canted with respect to the plane of the bipyridyl fragment, although not to the extent found for the mesityl system (Figure 4). This conformation presumably reflects the effect of van der Waals contacts of the hydrogen atoms ortho to the C−C link between the two rings.

One problem with using a crystal structure to interpret data collected in fluid solution is the potential influence of crystal lattice forces in determining the conformation of the phenyl rings in the solid state. Although an examination of a packing diagram does not reveal any obvious interaction that would force an otherwise planar phenyl ring into its observed canted position, we must nonetheless acknowledge it as a possibility. We do have additional evidence that strongly supports the notion that the canting of the phenyl ring in the dpb ground state is an intrinsic property of the molecule and not an artifact of the solid-state structure. We have used ab initio calculations to look at the ground-state structure in what is effectively the gas phase. Again, it was unfeasible to treat phenyl-substituted bipyridines with the basis sets reported herein, so the neutral 4-phenylpyridine served as a model for a ground-state ligand. As was mentioned, considerable effort has been spent on the theoretical treatment of biphenyl, its radical cation, and its radical anion.

(81) Jaffe, H. H.; Orchin, M. *Theory and Applications of Ultraviolet Spectroscopy*; John Wiley and Sons, Inc.: New York, 1962.

(82) Ohno, T.; Yoshimura, A.; Prasad, D. R.; Hoffman, M. Z. *J. Phys. Chem.* **1991**, *95*, 4723.

Table 8. Ab Initio Calculations on Neutral 4-Phenylpyridine

method/basis set	energy (hartrees) θ = optimized twist angle (NIMAG)[a]	$\Delta E_\theta°$ (NIMAG)[a]	$\Delta E_{90}°$ (NIMAG)[a]
RHF/3-21G(d)	−473.581779 $\theta = 50.1°$	3.29 kcal/mol	0.911 kcal/mol
	(0)	(1)	(1)
RHF/6-31G(d)	−476.247477 $\theta = 44.3°$	2.67 kcal/mol	1.62 kcal/mol
	(0)	(1)	(1)
MP2/6-31G(d)	−477.793958 $\theta = 44.6$	3.31 kcal/mol	1.80 kcal/mol
		(1)	(1)

[a] NIMAG = number of imaginary frequencies.

Recently, Rubio et al. have published a CASSCF/DZP study of neutral biphenyl where they report that the twist angle (θ) between the two ring systems of the biphenyl sits at 44.34°.[69] This result is in relatively close agreement with an earlier theoretical treatment by Tsuzuki et al., who report $\theta = 46.26°$ using Hartree−Fock theory and a 6-31G(p,d) basis set.[72] Electron diffraction techniques were used by Almenningen et al. to determine the gas-phase structure of biphenyl and suggest, in good agreement, a twist angle of 44.4°.[83] We have used Hartree−Fock methods and second-order perturbation theory to determine the geometry of neutral 4-phenylpyridine, especially in regards to the twist angle between the pyridyl and aryl ring systems. In addition, we have determined the barriers to rotation about the central 4,7 carbon−carbon bond.

Table 8 indicates that for the three method/basis set combinations, the lowest energy structure of 4-phenylpyridine is twisted. The geometry optimization with the smallest basis set (RHF/3-21G(d)) may have overestimated the twist angle at $\theta = 50.1°$; however, both calculations with the 6-31G(d) basis set are in close agreement with each other ($\theta = 44.3°$, 44.6°). We note the similarity between the calculated twist angle(s) of 4-phenylpyridine and those discussed above for biphenyl. The frequency calculations done with Hartree−Fock theory show that there are zero imaginary frequencies for the canted 4-phenylpyridine structures, indicating that these are indeed stationary minima. By symmetry, the coplanar ($\theta = 0°$) and the perpendicular ($\theta = 90°$) structures are rotational transition states. This is confirmed via Hartree−Fock frequency calculations where the number of imaginary frequencies for these geometries is one. MP2 frequency calculations were not attempted due to the computational cost involved, and they do not appear to be necessary. The coplanar barrier to rotation of 3.31 kcal/mol, as calculated with the MP2/6-31G(d) method/basis set, is significantly above room temperature thermal energy ($k_BT = 0.592$ kcal/mol at 298 K). These results indicate that the ground-state geometry of 4-phenylpyridine is an energetic compromise between the stabilization of increased delocalization and the destabilization of steric repulsion between opposing protons ortho to the bridging carbons. These calculations, in addition to suggesting a canted ground-state geometry for dpb, also serve to underscore the stabilization afforded by extended delocalization in the reduced species in that the steric repulsion has to be overcome to achieve the observed planar configuration.

Both the crystal structure of $[Ru(dmb)_2(dpb)](PF_6)_2$ and the calculations described above indicate that the neutral dpb ligand has a canted geometry with respect to the 4,4′ phenyl rings. It was mentioned earlier that we would expect complete attenuation of delocalization effects in the limit of a 90° dihedral angle, i.e., complete orthogonality between the two ring π systems.

(83) Almenningen, A.; Bastiansen, O.; Fernholt, L.; Cyvin, B. N.; Cyvin, S. J.; Samdal, S. *J. Mol. Struct.* **1985**, *128*, 59.

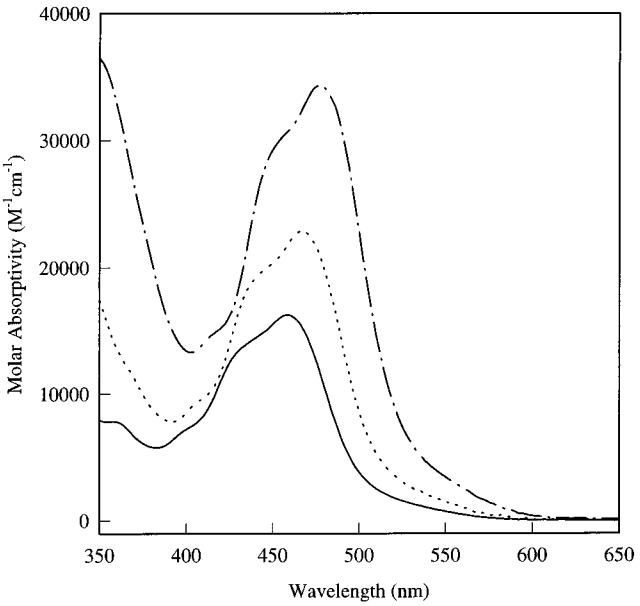

Figure 10. Absorption spectra of $[Ru(dmb)_3](PF_6)_2$ (solid line), $[Ru(dotb)_3](PF_6)_2$ (dotted line), and $[Ru(dptb)_3](PF_6)_2$ (dashed line) in CH_3CN solution.

This degree of orthogonality is clearly not achieved in $[Ru(dmb)_2(dpb)](PF_6)_2$, nor is the steric bulk of the methyl groups in dmesb quite sufficient to produce this situation, either. We can address the question of what extent delocalization is playing a role in the *ground state* of these complexes by examining both the solution-phase ground-state resonance Raman and electronic absorption spectra of the series. The ground-state resonance Raman spectra have already been discussed briefly. It was noted that the ground-state spectra of all of the complexes were strikingly similar. If we now compare these spectra to that of $[Ru(bpy)_3]^{2+}$ and $[Ru(dmb)_3]^{2+}$, we note that the overall pattern of the spectra is the same, suggesting that the same modes that are dominant in $[Ru(bpy)_3]^{2+}$ are also important in complexes of the dpb series. The only significant differences that are apparent occur in the frequencies of certain bands (e.g., the 1552 cm^{-1} band in $[Ru(dmb)_3]^{2+}$ versus 1539 cm^{-1} in $[Ru(dpb)_3]^{2+}$) associated with ring-stretch vibrations. This is suggestive of some degree of interaction between the peripheral phenyl rings and the pyridine rings, although without a normal coordinate analysis it is difficult to draw very definitive conclusions along these lines.

A more compelling indication of the presence of some extended π interaction in the ground-state electronic structure is available from electronic absorption data. The visible absorption spectra of $[Ru(dmesb)_3](PF_6)_2$, $[Ru(dotb)_3](PF_6)_2$, and $[Ru(dptb)_3](PF_6)_2$ in CH_3CN are illustrated in Figure 10. The most important point to note is the marked increase in ϵ upon phenylation of the bipyridyl rings, with the value at λ_{max} more than doubling between $[Ru(dmb)_3](PF_6)_2$ and $[Ru(dptb)_3](PF_6)_2$. Strictly speaking, what should be compared among these compounds are the oscillator strengths of the MLCT absorption manifolds. However, the fact that the overall shapes of the absorption profiles are all very similar (albeit shifted) suggests that a comparison of ϵ values at the λ_{max} for each compound will correlate reasonably well with the relative magnitudes of the oscillator strengths.

In general terms, the increase in ϵ upon going from $[Ru(dmb)_3](PF_6)_2$ to $[Ru(dptb)_3](PF_6)_2$ is reminiscent of the increase in radiative cross section observed in the excited-state data, suggesting a slight amount of electron delocalization (i.e., larger

transition dipole) in the ground states of these molecules. There is not as smooth a trend in the values of ϵ across the entire series as was observed for k_r and k_{nr}, but the molecules do tend to group together according to steric bulk: dmb, followed by dmesb and dotb, and finally dpb and dptb. It should be pointed out that ground-state absorption data reflect the Franck−Condon overlap between an excited state and the equilibrium geometry ground state. To accurately comment on trends in ϵ or oscillator strength, then, it would be necessary to know the degree of delocalization in the ^{1}MLCT Franck−Condon excited state *prior* to relaxation since this is not necessarily the same as the ground state. We hope to address this very issue using ultrafast absorption spectroscopy (vide infra).

Concluding Comments

The data in this paper have presented evidence for the formation of a planar excited-state conformation of the peripheral phenyl rings in $[Ru(dpb)_3](PF_6)_2$ following $^1MLCT \leftarrow {}^1A_1$ excitation. It has been further demonstrated that this planarity allows for intraligand electron delocalization in the MLCT excited state(s) of the compound, and that the extent of this delocalization and its subsequent effect on the photophysical properties of the molecule can be tuned through synthetic means. In addition, it has been established through crystallographic, spectroscopic, and computational methods that the planar motif is not the preferred geometry of the ground state. Rather, a canted structure is the ground-state conformation for each molecule in the series, including the sterically less encumbered dpb and dptb ligands. Finally, delocalization in the ground states of these molecules has been briefly examined. The data clearly support the notion that while there is evidence for some delocalization involving the phenyl rings in the ground states of these molecules, the extent of delocalization still markedly increases in the ^{3}MLCT excited state. Moreover, the extent of the ground-state delocalization and consequently the degree of increase upon excited-state formation can be roughly predicted and ultimately controlled by manipulation of steric factors.

When combined into an overall picture for excited-state evolution, some very interesting issues arise. The results we have presented can be viewed in terms of a strong coupling between electronic and steric factors in the excited states of these molecules. Specifically, we have shown that the extent of electronic delocalization can be modulated by altering the geometric constraints of the system. This coupling of electronic structure to nuclear configuration is the essence of vibronic coupling. However, in this instance, the vibronic coupling occurs between excited state surfaces, i.e., the Franck−Condon state of the molecule and the electronically and vibrationally relaxed ^{3}MLCT excited state. Excited-state evolution in these compounds therefore represents an instance in which the dynamics of electronic relaxation are truly dependent upon nuclear rearrangement in the excited state. Insight into this process can be gleaned from the calculations presented on the neutral and reduced 4-phenylpyridine presented above. These calculations effectively represent an energetic model of the Franck−Condon state that would be produced if the neutral ligand were suddenly reduced by a charge transfer transition. As indicated in Table 5, there is a considerable driving force ($\Delta E_\theta \sim 7$ kcal/mol) to achieve planarity from this twisted "Franck−Condon" state:

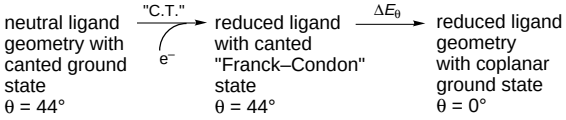

This, then, appears to be an important driving force for nuclear rearrangement in the excited state, but a consequence of this is that the dynamics of electron delocalization are going to be dictated in large part by the dynamics of nuclear rearrangement and vice versa.

In terms of the vibronic coupling that clearly must be operative in these systems, an interesting point to note is the fact that the mode to which excited-state evolution is coupled would appear to be the C−C bond rotation at the 4 position of the pyridyl ring. This is *not* believed to be an important mode for $^3MLCT \rightarrow {}^1A_1$ relaxation as shown from the spectral fitting analysis (vide supra)[84] suggesting that $^1MLCT \rightarrow {}^3MLCT$ conversion occurs along a different nuclear coordinate than $^3MLCT \rightarrow {}^1A_1$ relaxation. To our knowledge, there has been no detailed discussion about the nature of vibronic coupling for this initial step in excited-state evolution in this class of molecules. In any event, we believe that complete electronic relaxation might be "slowed down" in our systems because of excited-state vibronic coupling and the necessity for achieving a planar ligand conformation in order to realize a fully delocalized excited state. If this is the case, then the optical signature for the planar, thermalized excited state (vide supra) suggests the use of transient absorption spectroscopy to time-resolve the onset of extended electronic delocalization in the excited states of these molecules. Preliminary femtosecond absorption measurements on $[Ru(dpb)_3]^{2+}$ have revealed that this is, in fact, possible[85] and we will be reporting the full details of the ultrafast spectroscopy of these systems in the near future.

Acknowledgment. The authors wish to thank Professor Robert Damrauer of the University of Colorado at Denver for use of the Alpha workstation for ab initio calculations, Professor Thomas J. Meyer of the University of North Carolina at Chapel Hill for access to the apparatus for time-resolved resonance Raman spectroscopy, and Dr. Earl Danielson for assistance with the electronics and data acquisition software. This research was supported by the Division of Chemical Sciences, Office of Basic Energy Sciences, Office of Energy Research, U.S. Department of Energy, Grant No. DE-FG03-96ER14665, and the American Chemical Society Petroleum Research Fund, Grant No. 31016-G6.

Supporting Information Available: Supporting crystallographic tables (positional parameters and thermal parameters) for $[Ru(dmesb)_3](PF_6)_2$ and $[Ru(dmb)_2(dpb)](PF_6)_2$ as well as Raman band energies and electronic absorption data for the full series of molecules (14 pages). See any current masthead page for ordering and Internet access instructions.

JA971321M

(84) It should be noted that such a torsional mode would be expected to occur at very low frequency and would be difficult to observe. This mode must become active at some stage to reformulate the canted ground state, but it is unclear whether it plays a role as an acceptor in the relaxation mechanism.

(85) Damrauer, N. H.; McCusker, J. K. Unpublished results.